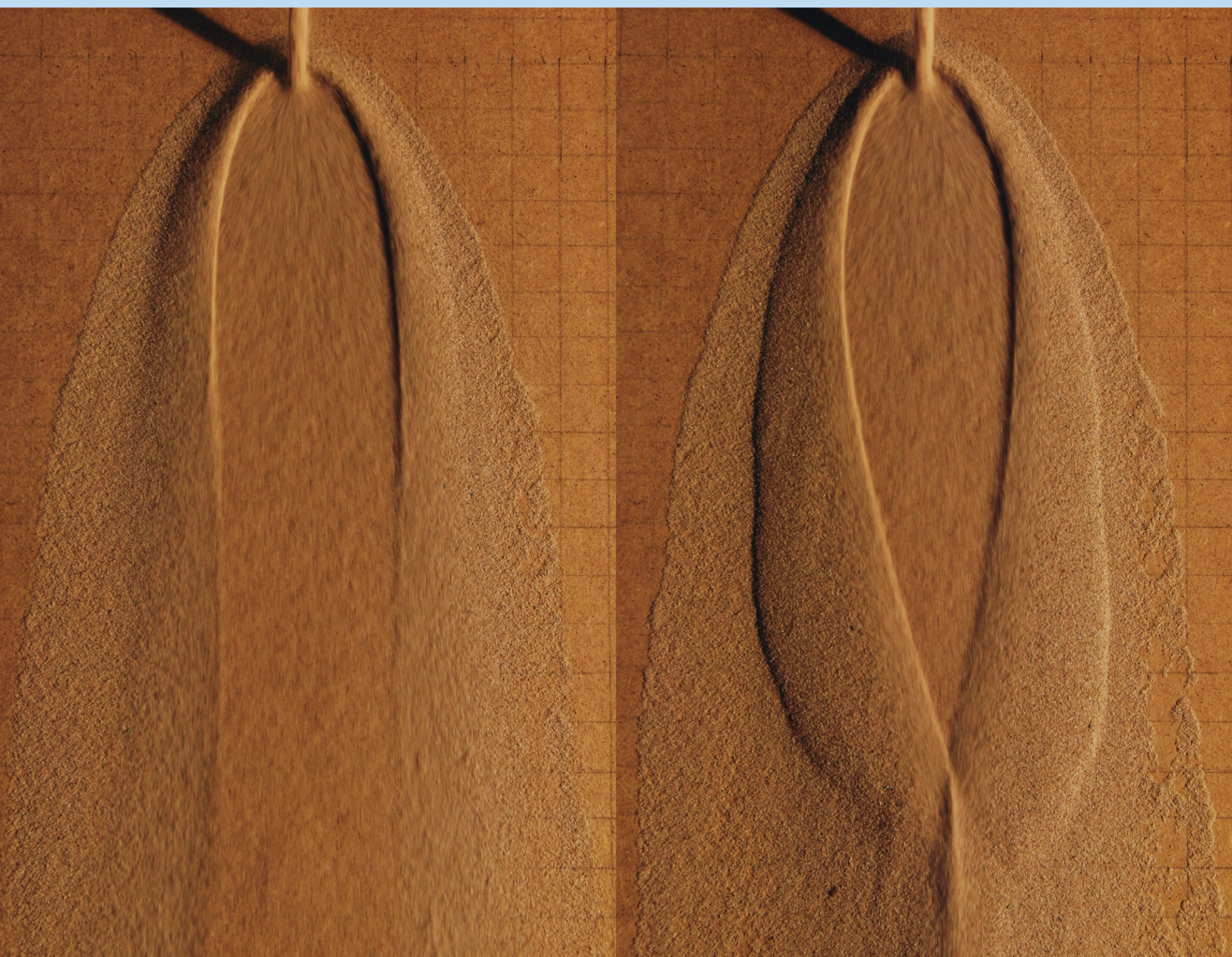


CAMBRIDGE
UNIVERSITY PRESS

25 May 2011

Journal of Fluid Mechanics

VOLUME 675



Granular jets and hydraulic jumps on an inclined plane

C. G. JOHNSON† AND J. M. N. T. GRAY

School of Mathematics and Manchester Centre for Nonlinear Dynamics, University of Manchester,
Oxford Road, Manchester M13 9PL, UK

(Received 7 October 2009; revised 26 July 2010; accepted 22 December 2010;
first published online 18 April 2011)

A jet of granular material impinging on an inclined plane produces a diverse range of flows, from steady hydraulic jumps to periodic avalanches, self-channelised flows and pile collapse behaviour. We describe the various flow regimes and study in detail a steady-state flow, in which the jet generates a closed teardrop-shaped hydraulic jump on the plane, enclosing a region of fast-moving radial flow. On shallower slopes, a second steady regime exists in which the shock is not teardrop-shaped, but exhibits a more complex ‘blunted’ shape with a steadily breaking wave. We explain these regimes by consideration of the supercritical or subcritical nature of the flow surrounding the shock. A model is developed in which the impact of the jet on the inclined plane is treated as an inviscid flow, which is then coupled to a depth-integrated model for the resulting thin granular avalanche on the inclined plane. Numerical simulations produce a flow regime diagram strikingly similar to that obtained in experiments, with the model correctly reproducing the regimes and their dependence on the jet velocity and slope angle. The size and shape of the steady experimental shocks and the location of sub- and supercritical flow regions are also both accurately predicted. We find that the physics underlying the rapid flow inside the shock is dominated by depth-averaged mass and momentum transport, with granular friction, pressure gradients and three-dimensional aspects of the flow having comparatively little effect. Further downstream, the flow is governed by a friction–gravity balance, and some flow features, such as a persistent indentation in the free surface, are not reproduced in the numerical solutions. On planes inclined at a shallow angle, the effect of stationary granular material becomes important in the flow evolution, and oscillatory and more general time-dependent flows are observed. The hysteretic transition between static and dynamic friction leads to two phenomena observed in the flows: unsteady avalanching behaviour, and the feedback from static grains on the flowing region, leading to levéed, self-channelised flows.

Key words: granular media, shallow water flows, shock waves

1. Introduction

It is a familiar observation that a jet of fluid impinging normally on a horizontal plane generates a thin, circular region of rapid radial flow surrounded by a stationary hydraulic jump, beyond which lies a thicker, slower moving fluid layer. The first analysis of this situation, in the case of inviscid fluid, is due to Lord Rayleigh

† Email address for correspondence: cjohnson@maths.manchester.ac.uk

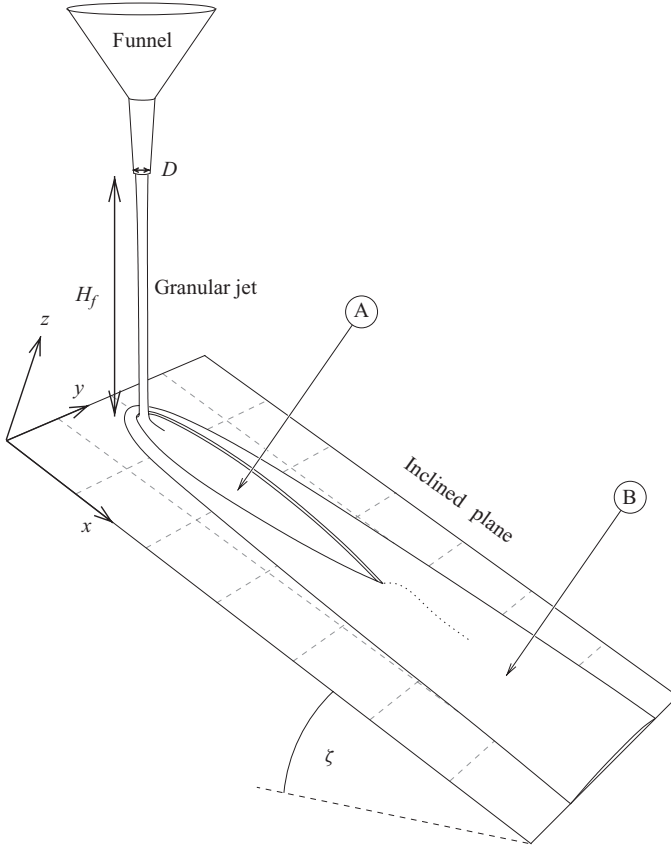


FIGURE 1. Diagram of the experimental apparatus. The granular jet impinges on the inclined plane, spreading into a region of thin, fast flow (A). The granular material then passes through a jump, becoming thicker and slower (B) and flows down the plane, which is inclined at an angle ζ to the horizontal.

(1914). The problem has since been extensively studied, and has been generalised to cover various fluid-dynamical phenomena such as viscosity (Watson 1964), internal interfaces (Thorpe & Kavcic 2008), non-Newtonian rheology (Zhao & Khayat 2008) and surface tension (Bush & Aristoff 2003). We examine in this paper the related situation of a vertical jet of granular material impinging on an inclined plane, shown schematically in figure 1. There are three key differences from Rayleigh's analysis: the flow of grains rather than of fluid, the impingement of the jet at an oblique angle and the effect of gravity on the flow down the inclined plane.

Several related problems of jet impingement and subsequent flow have previously been considered. The oblique impact of a fluid jet on a horizontal surface is described by Kate, Das & Chakraborty (2007), who observe the circular hydraulic jump of Rayleigh in flows generated by a vertical fluid jet, and an elliptical hydraulic jump for jets with impingement angles within 65° from normal. For angles greater than this, when the jet impinges near-tangentially, closed hydraulic jumps with sharp corners are observed. These are attributed to two phenomena: the interaction of the jet with the hydraulic jump and, by analogy with compression shocks of gas dynamics, the presence of Mach stems. Edwards *et al.* (2008) consider theoretically the normal impingement of a fluid jet on a plane inclined at an angle. In this situation, the

predicted hydraulic jump is not closed, but instead forms an open curve resembling a parabola. The flow is similar to the sheet of flow generated by two symmetric impinging jets (Taylor 1960; Bush & Hasha 2004), in that the more slowly-moving fluid outside of the shock forms a tube-like structure, which is small in width compared to the size of the enclosed thin film. This separation of scales is exploited to model the outer region as a ‘mass tube’, a line initially of unknown position, which carries mass and momentum fluxes. Coupling this to analytic solutions of a shallow-water model for the inner fast-moving region allows the location of the shock to be calculated. In the granular case, the problem of a jet of sand impinging normally on a horizontal plane is examined experimentally by Boudet *et al.* (2007). The behaviour found is similar to that in the fluid case, in that the granular jet transitions to a thin, fast, radial flow on impact with the plane, which is bounded by an annular jump in the layer thickness. In contrast to the fluid behaviour, the basal friction between the granular material and the horizontal plane slows the radial flow, and leads to the material outside the jump becoming stationary. The jump then propagates inwards, towards the point of jet impact.

Interest in the granular problem, and in granular flows in general, stems from the widespread use of granular materials, and the considerable problems encountered in understanding their behaviour. The flow of granular materials is central to the modelling of debris-flows (Iverson 1997) and snow avalanches (Cui, Gray & Jóhannesson 2007; Gruber & Bartelt 2007) in geophysics, to problems of transport, mixing and crushing of grains and powders in industry and to problems of soil stability and mechanics (Mitchell & Soga 2005) in civil engineering. Granular materials exhibit a wide range of behaviour, including solid-like, liquid-like and gas-like states, depending on factors such as grain density, granular temperature and shear stress (Liu & Nagel 1998; Rajchenbach 2000).

2. Governing equations of shallow granular flows

Granular flows of small aspect ratio (those in which the flow depth is much less than its horizontal extent) are common in free-surface flows on an inclined surface, whether at laboratory or geophysical scales. Such flows have been successfully modelled using shallow-layer models (Grigoryan, Eglit & Yakimov 1967; Eglit 1983; Savage & Hutter 1989; Gray, Wieland & Hutter 1999). A major difference between these depth-averaged models and fluid hydraulic or shallow-water systems is in the form of friction present at the base of the granular flow, either a Coulomb friction for smooth slopes (Savage & Hutter 1989) or a more complex friction model (that of Pouliquen & Forterre 2002, for example) for dry granular flows on rough slopes. Such friction laws, in contrast to viscous or turbulent friction modelling in shallow fluid layers, have the ability to hold a pile of material stationary on an inclined surface.

In common with the fluid-dynamical case, the hyperbolic equations of shallow-layer granular flow predict the formation of shocks, which correspond to *granular jumps*, the granular analogue of hydraulic jumps. These have been observed and studied in dense granular avalanches in chutes (Savage 1979; Brennen, Sieck & Paslaski 1983) and in flowing surface layers (Gray & Hutter 1997). More recently, two-dimensional oblique shocks have been observed in granular avalanches (Gray, Tai & Noelle 2003), which are quantitatively predicted by a similar analysis to that of hydraulic theory (Rouse 1949; Hákonardóttir & Hogg 2005; Gray & Cui 2007; Vreman *et al.* 2007). Density, or compression shocks have also been observed in granular materials, both in the regime of a granular gas (Rericha *et al.* 2002), where they are analogous to the

shocks observed in compressible gas dynamics, and in dense avalanche flows (Eglington, Kulibaba & Naaim 2007).

In a shallow-avalanche model, the flow is assumed to be incompressible, and is represented in terms of its depth-averaged velocity \mathbf{u} and height h . The governing equations are those of conservation of mass and momentum. Our coordinate system is defined such that the x -axis is oriented in the downslope direction, the y -axis in the cross-slope direction and the z -axis is the upward pointing normal to the plane, completing a right-handed Cartesian coordinate system (figure 1) with the origin at the point of jet impingement. The components of the velocity \mathbf{u} in the x and y directions are denoted u and v , respectively.

We present the equations in the non-dimensional form of Savage & Hutter (1989). Dimensional variables, denoted by a tilde, are related to their non-dimensional counterparts by the equations

$$\tilde{h} = Hh, \quad (\tilde{x}, \tilde{y}) = L(x, y), \quad (\tilde{u}, \tilde{v}) = \sqrt{L/g}(u, v), \quad \tilde{t} = \sqrt{L/g}t, \quad (2.1)$$

where H and L are typical length scales of the flow thickness and horizontal extent, respectively. Defining the small aspect ratio $\epsilon = H/L$, the non-dimensional equations for conservation of mass and momentum in the x and y directions are then (Gray *et al.* 2003)

$$\frac{\partial h}{\partial t} + \frac{\partial}{\partial x}(hu) + \frac{\partial}{\partial y}(hv) = 0, \quad (2.2)$$

$$\frac{\partial}{\partial t}(hu) + \frac{\partial}{\partial x}(hu^2) + \frac{\partial}{\partial y}(huv) + \frac{\partial}{\partial x}\left(\frac{1}{2}\epsilon h^2 \cos \zeta\right) = hs_x, \quad (2.3)$$

$$\frac{\partial}{\partial t}(hv) + \frac{\partial}{\partial x}(huv) + \frac{\partial}{\partial y}(hv^2) + \frac{\partial}{\partial y}\left(\frac{1}{2}\epsilon h^2 \cos \zeta\right) = hs_y. \quad (2.4)$$

The source terms

$$s_x = -\mu \frac{u}{|\mathbf{u}|} \cos \zeta + \sin \zeta, \quad (2.5)$$

$$s_y = -\mu \frac{v}{|\mathbf{u}|} \cos \zeta, \quad (2.6)$$

encompass both the effects of friction between the material and the inclined plane (through the basal friction coefficient μ), and the component of gravity in the x -direction.

Note that if we define $\hat{h} = \epsilon h$, then (2.2)–(2.6) can be rewritten in terms of the variables (\hat{h}, \mathbf{u}) in a form that is completely independent of ϵ . The parameter ϵ may therefore be chosen arbitrarily. Here, however we use the scalings (2.1) and retain ϵ in the equations to emphasise that the dominant balance in the avalanche equations is between the acceleration and source terms.

A Froude number

$$Fr = \frac{|\mathbf{u}|}{\sqrt{h\epsilon \cos \zeta}} \quad (2.7)$$

is defined as the ratio of flow speed to the speed of inertia-gravity waves. In steady flows, the Froude number relates directly to the way information is propagated by these waves. Information, in the form of small disturbances, is able to propagate in all directions in subcritical regions, where $Fr < 1$. In supercritical regions, where $Fr > 1$, information is unable to propagate against the direction of the flow (Courant & Hilbert 1962; Weiyan 1992). In supercritical flows, the hyperbolic structure of the equations allows for discontinuities in the solution, or shocks, at which the assumption

of smoothness implicit in the formulation of (2.2)–(2.4) is invalid. A relationship between the solution values on either side of the shock is instead given by the jump conditions

$$[\![h(\mathbf{u} \cdot \mathbf{n} - v_n)]\!] = 0, \quad (2.8)$$

$$[\![hu(\mathbf{u} \cdot \mathbf{n} - v_n) + \frac{1}{2}\epsilon h^2 \cos \zeta \mathbf{n}]\!] = 0, \quad (2.9)$$

derived from the mass and momentum conservation equations in integral form. The jump bracket $[\![\cdot]\!]$ denotes the change in continuum variables over a shock, \mathbf{n} is a unit vector normal to the shock and v_n is the shock speed.

3. Experimental observations

Our experimental setup is shown in figure 1. A funnel with a circular mouth of diameter D , in the range 8–15 mm, is held at a distance H_f above an inclined plane. Granular material flowing from the funnel impinges on the inclined plane and generates a thin free-surface flow, or avalanche, on the plane. The surface of the plane is made of untreated hardboard, which is rough at scales below approximately 100 µm. The funnel is fed from another hopper with larger flow rate to prevent variations in the supplied mass flux caused by a varying level of material in the lower funnel. The variation in mass flux delivered by the funnels, measured across 0.6 s samples, is less than 1.6 %. We observe no long-term variability in the flow (caused for example by changing environmental conditions) in this set-up.

The granular material used in the experiments presented in this paper is soft masonry sand, sieved to a diameter $d \leq 600$ µm. The experiments were also performed with glass ‘deco’ beads of two sizes, $75 \leq d \leq 150$ µm and $500 \leq d \leq 750$ µm, and with nonpareil sugar grains with $d \approx 1000$ µm. The flow on the plane is qualitatively independent of the type of granular material, exhibiting the same regimes of flow for all the materials tried. The flow in the region where the jet impacts the plane, however, is sensitive to particle properties. A small proportion of the granular material falling from the funnel does not transition to flow over the inclined plane at the point of impingement, but instead bounces off the plane, forming a sparse cloud of fast-moving grains. This proportion increases with funnel height (a behaviour attributable to the decreasing density of the jet as it falls) and becomes the dominant behaviour of the flow for sufficiently large H_f . For glass beads and sugar grains, a substantial proportion of the jet becomes airborne when $H_f \gtrsim 15$ cm (for $D = 15$ mm), a sufficiently low height that flows can be observed only in a very restricted parameter space. The corresponding maximum H_f for sand is much higher, approximately 50 cm. Results are therefore presented only for sand in this paper. The maximum funnel height is also limited by a clustering instability in falling granular jets, resembling that of the Rayleigh–Plateau instability for fluids (Royer *et al.* 2009). The instability has its onset at a distance greater than 50 cm from the funnel for $D \geq 8$ mm, and is therefore not a significant source of mass flux variation in the current experiment. For the range of funnel widths used, the requirement that the flow transitions smoothly to a flow over the inclined plane restricts the maximum H_f to a lower level than that enforced by the onset of the jet instability.

We consider primarily the flow after its impact with the plane. Depending on the slope angle, funnel height and funnel width, this flow exhibits a wide range of behaviours, resulting from the interaction between the momentum imparted to the flow by the falling granular material, friction between the plane and the granular material, and gravity.

3.1. Steady teardrop-shaped granular jumps

In the first flow regime, the falling jet generates a region of thin, fast-moving flow, which meets slower-moving material surrounding it at a granular jump. Boudet *et al.* (2007) demonstrated that on a horizontal plane, material behind this shock is stationary and the shock propagates inwards towards the point of impingement. However, for planes inclined at a sufficiently steep angle, the material flows on both sides of the granular jump, leading to a stationary granular jump surrounded by a steady flow.

Such a steady-state flow, for $\zeta = 26.7^\circ$ and $H_f = 30\text{ cm}$, is shown in figure 2. In the region of fast, thin supercritical flow within the shock, the flow velocity is predominantly radial, away from the point of impingement. Across the closed granular jump surrounding this region, the flow height rapidly increases and flow velocity normal to the shock rapidly decreases. In the region surrounding and downstream of the shock, grains flow more slowly, and largely in the downslope direction. In the flow shown in figure 2, the hydraulic jump is teardrop-shaped, with the shock displaying a single vertex directly downslope of the point of impingement.

The motion blur in still photographs of the experiment taken over a range of shutter speeds allows an estimation of surface flow velocities to be made, with an accuracy of about $\pm 10\%$. The thin radial flow surrounding the point of impingement has a speed of approximately 0.99 m s^{-1} . Substantial velocity variations exist in the thicker flow surrounding the jump, with the fastest velocities of approximately 0.4 m s^{-1} being observed close to the jump, where the flow is almost parallel to the line of the shock. This forms two fast-moving streams of material in the thicker flow, which meet at the vertex of the teardrop-shaped shock. At this oblique collision of the two streams, material is forced upwards into a narrow ‘spout’ normal to the inclined plane; this transfer of momentum to an orthogonal plane resembles that observed in the fluid chains generated by impinging fluid jets (Bush & Hasha 2004) or to the jets observed in shallow fluid flows at high Froude number (Edwards *et al.* 2008). A stream of fast-moving flow continues downstream of this, along the centreline of the flow. Far downstream, the centreline flow speed is approximately 0.11 m s^{-1} .

The thickness of the flow is of order 1 mm inside the shock, and 1 cm outside of it. This leads to Froude numbers of approximately 10 inside the shock, 1.4 in the fast-moving streams outside the shock, and 0.3 in the surrounding flow; the flow is therefore supercritical in a region including the shock, and transitions to subcritical flow downstream.

Figure 3 shows a time sequence of the formation of the teardrop-shaped shock. The first material to strike the plane spreads into a thin radially-flowing layer (figure 3a,b). This layer is slowed by friction and, upslope of the point of impingement, by gravity. The upslope flow becomes stationary approximately 0.25 s after the jet impact (figure 3c); this forms a shock in flow height that propagates inwards and wraps around the point of impingement (figure 3d,f) as the amount of granular material outside the shock increases. Unlike the case of impingement on a horizontal plane, material on both sides of the shock is flowing. The inward movement of the shocks causes them to collide after approximately 1.5 s, forming a closed shock. The slower material outside the shock forms a down-slope flow (figure 3g), which reaches a steady state (figure 3h).

In the initial stages of the flow, before the steady state is reached, a thin layer of stationary grains is deposited on the inclined plane outside the flowing region. These particles, labelled in figure 2, have no effect on the flowing region: they can be brushed away without affecting the flow. The interface between flowing and stationary grains

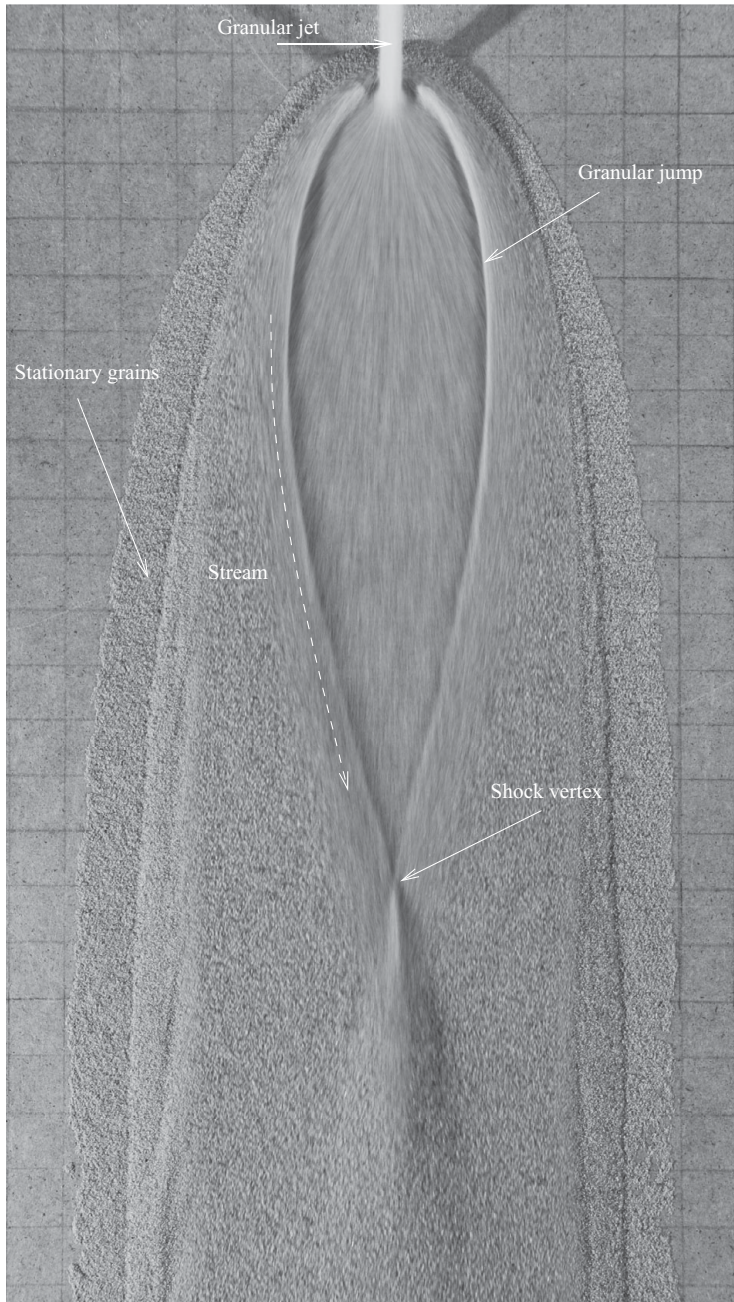


FIGURE 2. A teardrop-shaped shock in sand for $\zeta = 26.7^\circ$, $H_f = 30\text{ cm}$ and $D = 15\text{ mm}$. Grid squares are at 2 cm intervals, in this and subsequent figures. The shutter speed is 1/80 s.

exhibits small stick-slip fluctuations in all flows. However, in the flows described up to § 6, these fluctuations have a negligible effect on the steady flow. Observation of the steady flows for 30 min showed continued small fluctuations, but no long-term evolution of the flowing region.

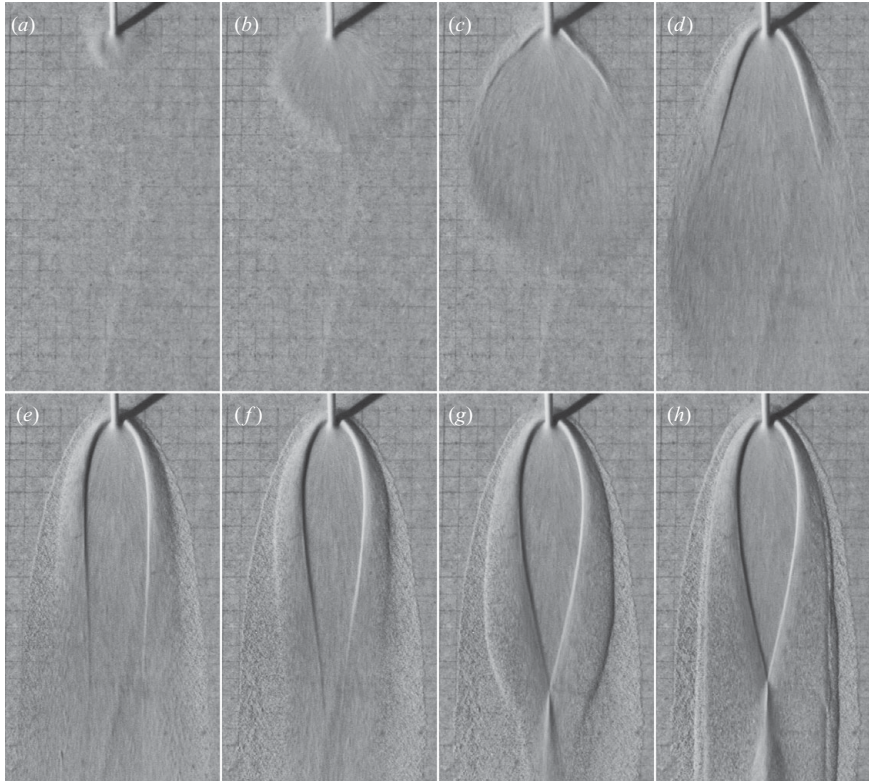


FIGURE 3. Time sequence of the formation of a teardrop-shaped shock, for $\zeta = 26.7^\circ$, $H_f = 30$ cm and $D = 15$ mm. Times after jet impact are: (a) 0.02 s, (b) 0.1 s, (c) 0.26 s, (d) 0.50 s, (e) 1.0 s, (f) 1.5 s, (g) 2.0 s and (h) steady-state. A movie showing the time-dependent evolution of this flow is available at journals.cambridge.org/film.

3.2. Steady blunted jumps

For shallower slope inclination angles, a second steady-state regime exists that displays the same radial flow inside a closed granular jump as before, but in which the shock is blunted, as shown in figure 4. The sharp vertex of the teardrop-shaped shock is replaced by a normal shock which lies across the slope. When the two streams of flow in the thicker layer of material adjoining the shock reach this normal shock, they are in part directed towards each other, following the line of the closed shock, and in part detach from the shock and decelerate rapidly to form part of the downslope flow. The speed of flow downstream of the shock is about 0.07 m s^{-1} .

In the centre of the cross-slope jump, a complex three-dimensional interaction between three flow streams is observed: the material from the inner region, flowing directly downstream, encounters both a normal shock, and the components of the two streams that have been diverted towards one another. The flow at the shock overturns, and resembles a static continuously breaking wave. The overturning of the flow at the shock has some resemblance to the recirculation observed in two-dimensional propagating granular bores by Gray *et al.* (2003). As a result of this interaction between the streams, the downstream flow is thickest in two broad regions either side of a thin trench along the axis of symmetry, a configuration which persists in the flow downstream. For smaller ζ and greater H_f , the region enclosed by the hydraulic jump becomes wider in the y -direction, and shorter in the x -direction; in

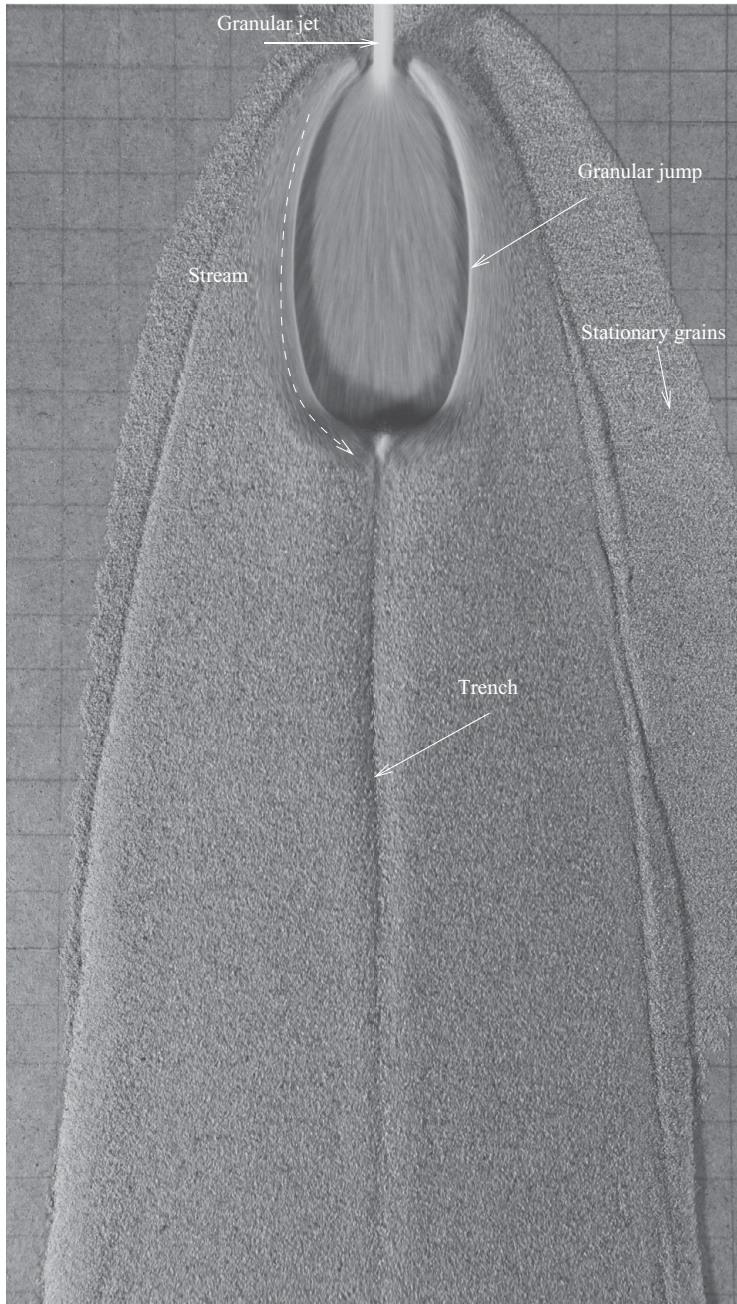


FIGURE 4. A blunted shock in sand, $\xi = 25.4^\circ$, $H_f = 30$ cm, $D = 15$ mm.
The shutter speed is 1/80 s.

this case, two parallel trenches can be generated, forming a w-shaped indentation in the downslope flow. A supplementary movie, available at journals.cambridge.org/film, shows the complex flow in this region.

A phase diagram of the flow regimes for $D = 50$ mm is shown in figure 5. Teardrop-shaped shocks (denoted by \times) are observed in all flows where $H_f > 10$ cm and

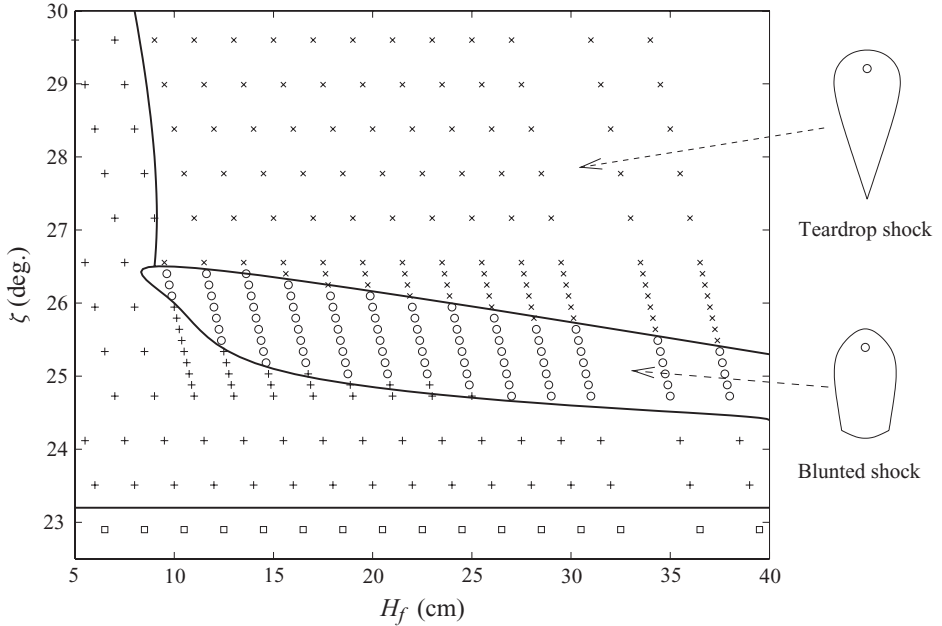


FIGURE 5. Experimental phase diagram, showing the dependence of flow regime on H_f and ξ , for $D=15$ mm. Teardrop-shaped shocks are indicated by crosses (\times), blunted shocks by circles (\circ) and steady flows with no shock by plus signs ($+$). Unstable time-dependent flows are represented by squares (\square). All flows for $\xi \gtrsim 23^\circ$ are steady.

$\xi > 26.5^\circ$; blunted shocks (denoted by \circ) are observed in a more limited range of slope angles, $24.5^\circ \lesssim \xi \lesssim 26.5^\circ$ and only for $H_f > 9$ cm. We attribute the different behaviour in the two regimes to whether the Froude number is greater or less than unity in the material immediately downstream of the radial flow region. This was determined experimentally by introducing a small disturbance onto the flow, for example with the point of a pin; if the flow is subcritical, the disturbance propagates in all directions, whereas for supercritical flow, the disturbance is limited to a wedge downstream of the pin. For teardrop-shaped shocks, the flow on the downstream side of the shock vertex is supercritical. Here, information can propagate only downstream, which explains the lack of visible influence of the shock interaction on the upstream flow, and the consequent sharp vertex. For blunted shocks, the material becomes subcritical as it passes through the cross-slope section of shock. In this subcritical flow, the effect of the collision between the shocks can propagate upstream, leading to the curved shock observed in experiments. The correspondence of Froude number with the flow regime is consistent with the observation that teardrop shocks occur at steeper slope inclinations, where the flow on the plane is faster and thinner (and thus of higher Froude number) than at lower inclinations. The decrease with increasing H_f of the critical slope inclination angle separating teardrop-shaped from blunted shocks (figure 5) is also consistent with this hypothesis, since the velocity of the flow at the inflow increases with H_f .

3.3. Other steady regimes

In addition to the blunted and teardrop-shaped shocks, two further regimes of steady-state flow exist in which a shock is not present. In the first of these, observed when $H_f \lesssim 10$ cm, the flow velocity in the region surrounding the impingement point is

still supercritical, but the shocks become sufficiently diffuse (that is, the variation in flow occurs over a sufficiently large region) that they are indistinguishable from the surrounding flow. This is consistent with the observation of Gray & Cui (2007) that shocks in granular materials become diffuse at low supercritical Froude numbers. The second regime occurs in the range of inclination angles $23^\circ \lesssim \zeta \lesssim 24.5^\circ$, when the flow is sufficiently deep that it is subcritical everywhere. Since supercritical flow is required for a hyperbolic shock to exist, this flow also displays no shocks. These steady flows without shocks are denoted by + signs in figure 5. Unsteady flows, observed for $\zeta \lesssim 23^\circ$ and denoted by \square , exhibit a wide range of complex behaviour which is discussed in § 6.

In addition to the hardboard surface of the inclined plane, the experiments were tried with two other surface types: a smooth perspex sheet, and a sheet of hardboard roughened by gluing a layer of sand to it. The teardrop-shaped shocks, as well as the steady and unsteady flows without shocks were observed on all surface types. On the roughened surface, blunted shocks were observed, with the transition between teardrop and blunted shock regimes occurring at $\zeta \approx 35^\circ$ and unsteady flows observed below approximately 30° . The increased friction on the roughened slope is responsible for the increase in slope angle required to balance friction in the steady flow downstream. On the perspex surface, the transition between teardrop-shaped shocks and unsteady flows occurs over a narrow range of slope angles close to 22° , with blunted shocks occurring only in this small region of parameter space. This transition is consistent with a constant Coulomb friction coefficient for the flow over a smooth surface.

4. Friction law and impingement condition

4.1. Friction law

We seek to model the experimental flows using the shallow-layer avalanche model of (2.2)–(2.6). The use of this model is motivated by the shallowness of the flows in question, in which the aspect ratio of the flow is approximately 1/30. To close the system of equations, an expression for the basal friction coefficient μ is required. The basal friction was taken to be a constant by Savage & Hutter (1989) for Coulomb-frictional flows over smooth surfaces. For such a friction law, steady flows of uniform thickness are possible only at a single slope angle, when $\zeta = \tan^{-1} \mu$. More recently, Pouliquen (1999b) performed laboratory-scale experiments of flows of glass beads over a roughened bed, and observed steady uniform flows over a range of slope angles. They demonstrated a minimum height $\tilde{h}_{stop}(\zeta)$ at which a steady flowing layer can exist on a slope inclined at an angle ζ , and found an empirical dependence of the ratio of flow height \tilde{h} to \tilde{h}_{stop} on the Froude number

$$Fr = \frac{|\mathbf{u}|}{\sqrt{h \epsilon \cos \zeta}} = \beta \frac{\tilde{h}}{\tilde{h}_{stop}(\zeta)}, \quad (4.1)$$

where $\beta = 0.136$ is a measured constant for glass beads. In one-dimensional steady uniform flows, the cross-slope velocity $v = 0$ and the downslope source term $s_x = 0$, leading to the relation between the friction coefficient and slope angle

$$\mu = \tan \zeta. \quad (4.2)$$

Denoting the inverse of $\tilde{h}_{stop}(\zeta)$ by $\zeta_{stop}(\tilde{h})$, the function

$$\mu_{stop}(\tilde{h}) = \tan(\zeta_{stop}(\tilde{h})), \quad (4.3)$$

leads, through the scaling law (4.1), to an equation for the friction coefficient

$$\mu = \tan \zeta = \mu_{stop}(\tilde{h}_{stop}(\zeta)) = \mu_{stop} \left(\frac{\tilde{h}\beta}{Fr} \right). \quad (4.4)$$

The form of the function μ_{stop} is a fit to the experimental measurements of $\tilde{h}_{stop}(\zeta)$, and takes the form of a transition between two friction angles ζ_1 and ζ_2 , either

$$\mu_{stop}(h') = \tan \zeta_1 + (\tan \zeta_2 - \tan \zeta_1) \frac{1}{1 + h'/\mathcal{L}}, \quad (4.5)$$

as in Pouliquen & Forterre (2002), or in the Pouliquen (1999b) form,

$$\mu_{stop}(h') = \tan \zeta_1 + (\tan \zeta_2 - \tan \zeta_1) \exp(-h'/\mathcal{L}). \quad (4.6)$$

The friction angles used here are those measured by Pouliquen & Forterre (2002), $\zeta_1 = 21^\circ$, $\zeta_2 = 30.7^\circ$, $\zeta_3 = 22.2^\circ$. The parameter \mathcal{L} , which has the dimensions of length, depends on the granular material and surface properties of the plane and characterises the depth of flow over which a transition between the two friction angles ζ_1 and ζ_2 occurs. The friction law (4.4) is valid for flows in the steady regime where $\tilde{h} > \tilde{h}_{stop}$, that is, for flows in which $Fr > \beta$.

For stationary material, the basal friction balances the lithostatic pressure and gravitational forces exactly, up to a maximum value corresponding to the coefficient of static friction $\mu = \mu_{start}(\tilde{h})$. This is calculated, through (4.2), by measuring the maximum inclination angle at which a uniform layer of stationary material starts to move, and takes the form

$$\mu_{start}(h') = \tan \zeta_3 + (\tan \zeta_2 - \tan \zeta_1) \frac{1}{1 + h'/\mathcal{L}}. \quad (4.7)$$

For flows of $0 < Fr < \beta$, we follow the method of Pouliquen & Forterre (2002) in interpolating between the static and steady-flow friction coefficients with a power function

$$\mu = \left(\frac{Fr}{\beta} \right)^\gamma (\mu_{stop}(\tilde{h}) - \mu_{start}(\tilde{h})) + \mu_{start}(\tilde{h}), \quad (4.8)$$

where $\gamma = 10^{-3}$. The parameter \mathcal{L} provides a convenient length scale with which to non-dimensionalise the depth of the flow. We take $\mathcal{L} = 10$ mm, and non-dimensionalise the flow depth by setting $H = \mathcal{L}$ in the scalings (2.1). The horizontal length scale for non-dimensionalisation L is chosen to be 0.5 m (a typical length of the closed granular jump and associated rapidly-flowing streams), giving $\epsilon = 1/50$.

The choice of a Pouliquen-type friction law rather than a Coulomb one is motivated by our observation of both steady uniform flows over a range of slope angles and a critical flow depth, dependent on slope angle, below which steady flow is not observed. In our simulations of the experiment, only small differences are found between results obtained with the friction law for glass beads, defined in (4.6) and (4.8) and a modified version for sand (Forterre & Pouliquen 2003, (4.17)).

Close-up photographs of the fast radially flowing region inside the shock show that the flow is only a few grains thick. This is consistent with the observations of Boudet *et al.* (2007), for the impingement of a jet onto a horizontal plane, where the flow is approximately four grain diameters deep. The flow in this region appears less dense than that in the more slowly flowing regions outside the shock, and than the material at the point of impingement itself. In the region of thin flow, many particles are not in contact with any other: the assumption of an incompressible continuum

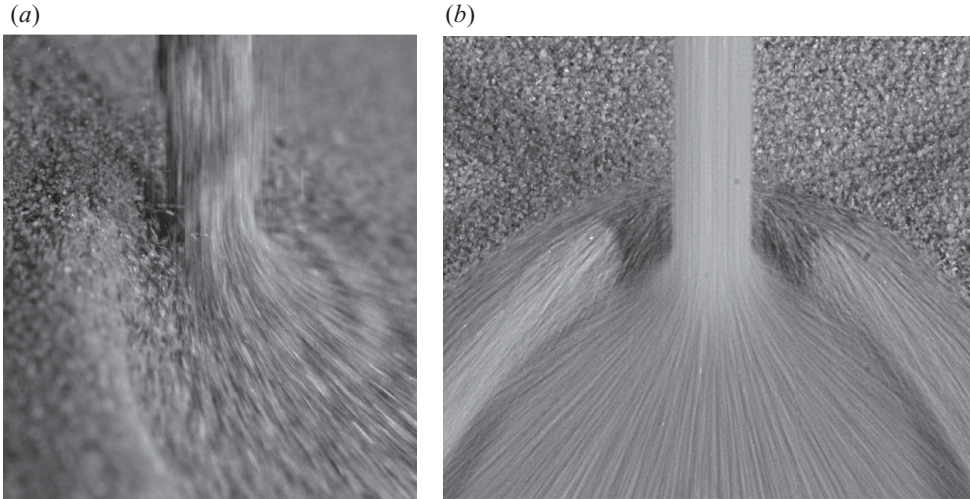


FIGURE 6. Photographs of the impingement region, viewing across the slope (*a*) and normal to it (*b*). The vertically falling jet of material is converted to a thin, radial flow on impact with the plane. Above the point of impingement, particles are held almost stationary by the dynamic pressure of material flowing uphill from the point of impingement.

is therefore invalid, and neither a lithostatic pressure nor a Pouliquen-type friction law would be expected here. These discrepancies are minimised by the small effect of internal pressure and basal friction in this region; the transport terms in (2.3)–(2.4) become large compared to the pressure gradient and frictional source terms. The exact choice of pressure and frictional models therefore has little effect in this region. Furthermore, the assumption of incompressibility can be relaxed by considering h not as the flow height, but as a measure of the amount of mass at a given point, as is possible when surface-gradient-generated pressures are negligible. While we might not expect h to accurately represent the flow height in this region of sparse flow (indeed, a flow height may not even be clearly defined), the mass and momentum fluxes are predicted correctly. Since these are the quantities which determine the shock relations, the use of the shallow avalanche model in the fast-moving region is acceptable for predictions of the shock position.

We model the internal stresses in the granular material as an isotropic lithostatic pressure, in contrast to the Mohr–Coulomb rheology used by Savage & Hutter (1989). Simulations of the current problem have been compared, with the earth-pressure coefficient firstly set to unity (e.g. Gray *et al.* 2003) in the isotropic case, and secondly determined by the two-dimensional formulation of Iverson & Denlinger (2001) in the case of a Mohr–Coulomb rheology. In the current problem, only small quantitative differences exist between the results of the two models; for simplicity, the isotropic pressure assumption is made.

4.2. Region of impingement

The region of impingement, in which the flow transitions from a vertical jet to flow across the inclined plane, is shown in detail in figure 6. The flow here is fully three-dimensional, and the approximations made in the assumption of shallow-layer flow are invalid. We seek an alternative model for the flow in this region, and match it to the shallow-layer model, which is valid elsewhere, by applying appropriate boundary conditions on an interface separating the two model regions.

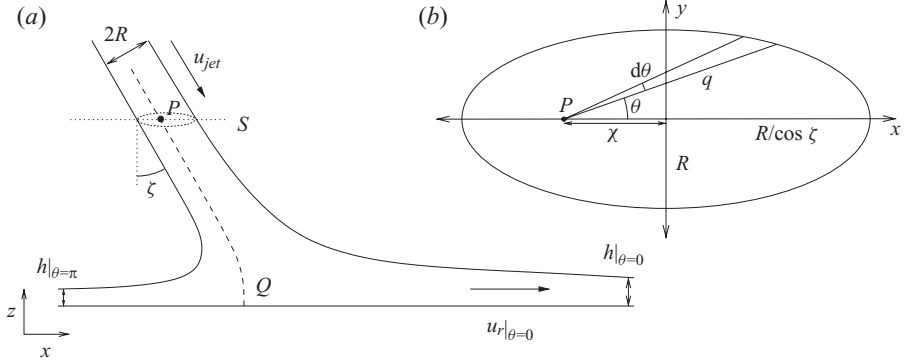


FIGURE 7. (a) Cross-section of the impingement region in the plane $y=0$. The separation streamline is shown as a dashed line. (b) Section of the jet in the plane S , parallel to the inclined plane

As in the case of the normal impingement examined by Boudet *et al.* (2007), a smooth transition from a falling jet of material to thin radial flow over a plane is observed, but details of the three-dimensional flow in the region of impingement are unknown. In the case of normal impingement, the problem resembles the high aspect-ratio limit of granular column collapse, a problem which has received extensive study (Lajeunesse, Mangeney-Castelnau & Vilotte 2004; Lube *et al.* 2004; Doyle *et al.* 2007). Contact dynamics simulations of this problem for column aspect ratios up to 17 (Staron & Hinch 2005) predict a smooth transition from falling to thin-layer flow. This is consistent with our experimental observations for a continuous stream. When a transparent plane is used to view the flow from beneath, a single stagnation point is observed under the jet, surrounded by a radial flow. For oblique impingements, the qualitative behaviour of the flow is similar, with a stagnation point observed under the jet impact region, surrounded by radial flow. The mass flux of the radial flow is no longer axisymmetric however, and becomes dependent on θ , the angle of a plane polar coordinate system in the xy -plane centred at the stagnation point.

In the absence of a granular rheology for this flow, we make the assumption that the flow in the region of impact can be modelled as an inviscid, irrotational and incompressible fluid. Under this assumption, the flow admits a solution which describes the transition of a jet of fluid to a radial flow across a plane (figure 7a). Our choice of this model is motivated by the qualitative similarity between its predictions and experimental observations. The granular impingement is subject to frictional energy losses, which are neglected in the ideal fluid model. An estimate of these losses in the case of normal impingement is given by Boudet *et al.* (2007), who found experimentally that the velocities in the radial flow generated by the normal impingement of a granular jet were 20 %–50 % lower than would be expected if energy were conserved in the region of impingement. Therefore, while the ideal fluid model is expected to correctly predict the distribution of granular material onto the plane, a quantitative link to the velocity of the falling jet is not attempted.

The oblique impingement of a circular jet of inviscid fluid on a plane was first described by Schach (1934). More recently, the analogous situation of two symmetric colliding jets has been considered, both experimentally (Taylor 1960) and theoretically (Hasson & Peck 1964). The flow contains a stagnation point Q on the plane, connected to the incoming jet by a separation streamline. We consider a section of the jet through

a plane S , parallel to the xy -plane and far from the impingement region (figure 7b), where the flow is parallel to the jet axis. The jet velocity through S is denoted u_{jet} . The jet is cylindrical and of radius R , and thus its intersection with S is an ellipse of major axis $2R/\sin\zeta$ in the x -direction and minor axis $2R$ in the y -direction. The intersection point of the separation streamline with S is denoted by P . Symmetry about the plane $y=0$ implies that P must lie on this plane, at a distance χ from the centre of the ellipse. The radial distance from the origin on the inclined plane is denoted r , and the radial velocity u_r .

Taylor (1966) showed that a full calculation of the three-dimensional flow in the region of impingement is required to determine how the outflow mass and momentum fluxes are distributed in θ . We follow Hasson & Peck (1964) in assuming that flow which enters the impingement region in the angular segment $d\theta$ (figure 7b) remains in this segment throughout the flow. This approximation is justified by good quantitative agreement with experimental results (e.g. Kate *et al.* 2007), and allows a solution for the outflow to be determined using global balance arguments alone. On this basis, we equate the mass flux through S in a segment $d\theta$ with the mass flux leaving the impingement region on the inclined plane in the same segment, giving

$$q d\theta \frac{q}{2} u_{jet} \cos \zeta = r d\theta h u_r, \quad (4.9)$$

where $q(\theta)$, defined in figure 7(b), is related to χ by the equation for an ellipse

$$(q \sin \theta)^2 + (q \cos \theta - \chi)^2 \cos^2 \zeta = R^2. \quad (4.10)$$

For radial flow far from the impingement region, the flow velocities in the z -direction are negligible. Applying Bernoulli's equation to a surface streamline then implies that the radial flow velocity u_r is equal to the jet velocity u_{jet} for all θ . The gravitational term in Bernoulli's equation can be neglected because the height of the impingement region H_{ir} is much smaller than the funnel height H_f ; the fractional change in velocity due to gravity within the impingement region, which scales like H_{ir}/H_f , is therefore small. With velocity in the radial flow equal to u_{jet} , (4.9) simplifies to

$$hr = \frac{q^2}{2} \cos \zeta. \quad (4.11)$$

The remaining unknown χ is calculated from the conservation of momentum in the x -direction. Considering x -momentum fluxes through S and in the radial flow gives

$$\rho \pi R^2 u_{jet}^2 \sin \zeta = \int_0^{2\pi} h \rho u_r^2 \cos \theta r d\theta, \quad (4.12)$$

which simplifies to

$$\pi \tan \zeta = \int_0^\pi \left(\frac{q}{R} \right)^2 \cos \theta d\theta. \quad (4.13)$$

Using (4.10) to evaluate q in terms of χ , if

$$\chi = R \tan \zeta, \quad (4.14)$$

then

$$q = \frac{R \cos \zeta}{1 - \sin \zeta \cos \theta}. \quad (4.15)$$

It can be shown that this expression for q satisfies (4.13), providing a solution for χ . Through (4.10) and (4.11), the solutions for \mathbf{u} and h at a distance r from the point of

separation are

$$\mathbf{u} = (u_{jet} \cos \theta, u_{jet} \sin \theta), \quad (4.16)$$

$$h = \frac{R^2 \cos^3 \zeta}{2r(1 - \sin \zeta \cos \theta)^2}. \quad (4.17)$$

This solution reproduces the observed stagnation point and, qualitatively, the dependence on θ and ζ of the radial mass flux for oblique impingement.

It remains to match the analytical solution found for the impingement region to the flow elsewhere, modelled by the shallow-layer equations (2.2)–(2.4). The values for \mathbf{u} and h given by (4.16) and (4.17) describe the solution of the inviscid jet impingement problem when r is sufficiently large that flow velocities in the z -direction are negligible. In addition, (4.16) and (4.17) are a solution of the shallow-layer model in the limits of no horizontal pressure gradients and source terms; these two limits are approached in the fast-moving flow of the impingement region. The boundary between the analytical solution in the impingement region and the surrounding shallow-water model is therefore chosen to be sufficiently far from the point of impingement that flow velocities in the z -direction are small, but sufficiently close to the point of impingement that frictional and pressure-driven accelerations on the flow within this region can also be neglected.

This assumes that the flow within the impingement region is not affected by the flow outside it. This is invalid if the flow is subcritical anywhere on the interface separating the two modelling regions, since information can then propagate from the flow outside back into the impingement region. The solution of the inviscid jet impingement problem (4.16)–(4.17) has Froude number increasing without bound for increasing radius; the condition of supercritical flow is therefore satisfied at sufficiently large r .

5. Numerical method and results

The system (2.2)–(2.4) is a set of nonlinear hyperbolic conservation laws that can be written in vector form as

$$\frac{\partial \mathbf{w}}{\partial t} + \frac{\partial \mathbf{f}(\mathbf{w})}{\partial x} + \frac{\partial \mathbf{g}(\mathbf{w})}{\partial y} = \mathbf{s}, \quad (5.1)$$

where $\mathbf{w} = (h, hu, hv)^T$ is the vector of conserved variables, and $\mathbf{s} = (0, hs_x, hs_y)^T$. The flux functions \mathbf{f} and \mathbf{g} are given by

$$\mathbf{f} = \begin{pmatrix} hu \\ hu^2 + \epsilon h^2/2 \\ huv \end{pmatrix}, \quad \mathbf{g} = \begin{pmatrix} hv \\ huv \\ hv^2 + \epsilon h^2/2 \end{pmatrix}. \quad (5.2)$$

Several techniques exist for the numerical solution of such systems of conservation laws (LeVeque 1992). We elect to solve the equations using the finite-volume method of Jiang & Tadmor (1998), an extension to two-dimensional Cartesian grids of the non-oscillatory central scheme of Nessyahu & Tadmor (1990). These methods are of high resolution, in the sense that flux limiters are used to obtain second-order accuracy away from the shocks, while remaining non-oscillatory in the region of discontinuities. For the numerical solutions presented here, the extended ‘MinMod’ limiter (Jiang & Tadmor 1998, (3.1)) has been used with parameter $\theta = 2$. The choice of conserved variables in the vector \mathbf{w} , in conjunction with the non-oscillatory scheme,

ensures that the numerical method is *shock-capturing*. Such methods are required to handle correctly the discontinuity in solution at a granular jump (Tai *et al.* 2001, 2002; Gray *et al.* 2003).

Downstream flow conditions strongly affect the formation of oblique shocks in granular flows (Gray & Cui 2007). In this problem, there are both sub- and supercritical regions present at the downstream boundary of the numerical domain, requiring either one or zero boundary conditions, respectively (Weiyan 1992, p. 111). This numerical boundary is treated by constructing a row of ghost cells outside the domain, with values determined by a linear extrapolation of the two final rows of interior cells, which is appropriate for both subcritical and supercritical outflow (LeVeque 2002, p. 131). This boundary is sufficiently far downstream that the numerical solution is independent of its exact position. The numerical domain has sufficient extent in the y -direction that all material leaving it does so through the downstream boundary.

In order to apply the boundary conditions at the matching interface between the solution for the impingement region given by (4.16) and (4.17) and the shallow-layer model elsewhere, we enforce (4.16) and (4.17) in any finite volume cells which lie within a circular region of radius R_{imp} , centred on the stagnation point Q . Since the impingement region solution and shallow-layer model solutions coincide here, the numerical solutions are expected to be insensitive to the point at which the two solutions are matched, provided that the conditions for the matching are satisfied. These conditions are that the velocities in the z -direction in the inviscid fluid model and horizontal pressure gradients and source terms in the shallow-layer model are negligible, and that the flow is supercritical everywhere on $r = R_{imp}$. The value $R_{imp} \approx 2R$ has been chosen, which satisfies these conditions for the simulated flow parameters. As expected, our numerical results are insensitive to the exact value of R_{imp} .

5.1. Teardrop-shaped shock

Figure 8 shows a numerical solution of (2.2)–(2.4) exhibiting a steady teardrop-shaped shock, comparable to that seen in the experimental flow of figure 2. The slope inclination angle and funnel diameter are the same as those in the experimental flow, and the axes of figure 8 cover the same region as that shown in figure 2.

The unknown energy loss in the impingement region means that the funnel heights H_f in numerical solutions are not directly comparable to those in the experiments. Instead, the speed of the radial flow inside the shock is compared. Under the ideal fluid model for the impingement region, (4.16) implies that the speed of flow leaving the impingement region on the inclined plane is u_{jet} . Experimentally, we estimate this velocity to be approximately 0.99 m s^{-1} in figure 2: we therefore use $u_{jet} = 0.99 \text{ m s}^{-1}$ for the numerical solutions in figures 8–10.

Figure 8(a) shows the location of the shock as a black line, with streamlines of the flow in grey. The region in which the flow is supercritical is shaded. The numerical solution reproduces well the region of fast radial flow surrounding the point of impingement (indicated by radial streamlines), the teardrop-shaped shock and the shape of the flowing region. The shock length is 0.28 m, close to the experimental result of 0.27 m.

The shaded region of supercritical flow outside the shock shows that the two supercritical streams on either side of the teardrop merge at the shock vertex to form a single stream. This is consistent with the experimentally observed region of supercritical flow in figure 2, which approximately corresponds to the region of

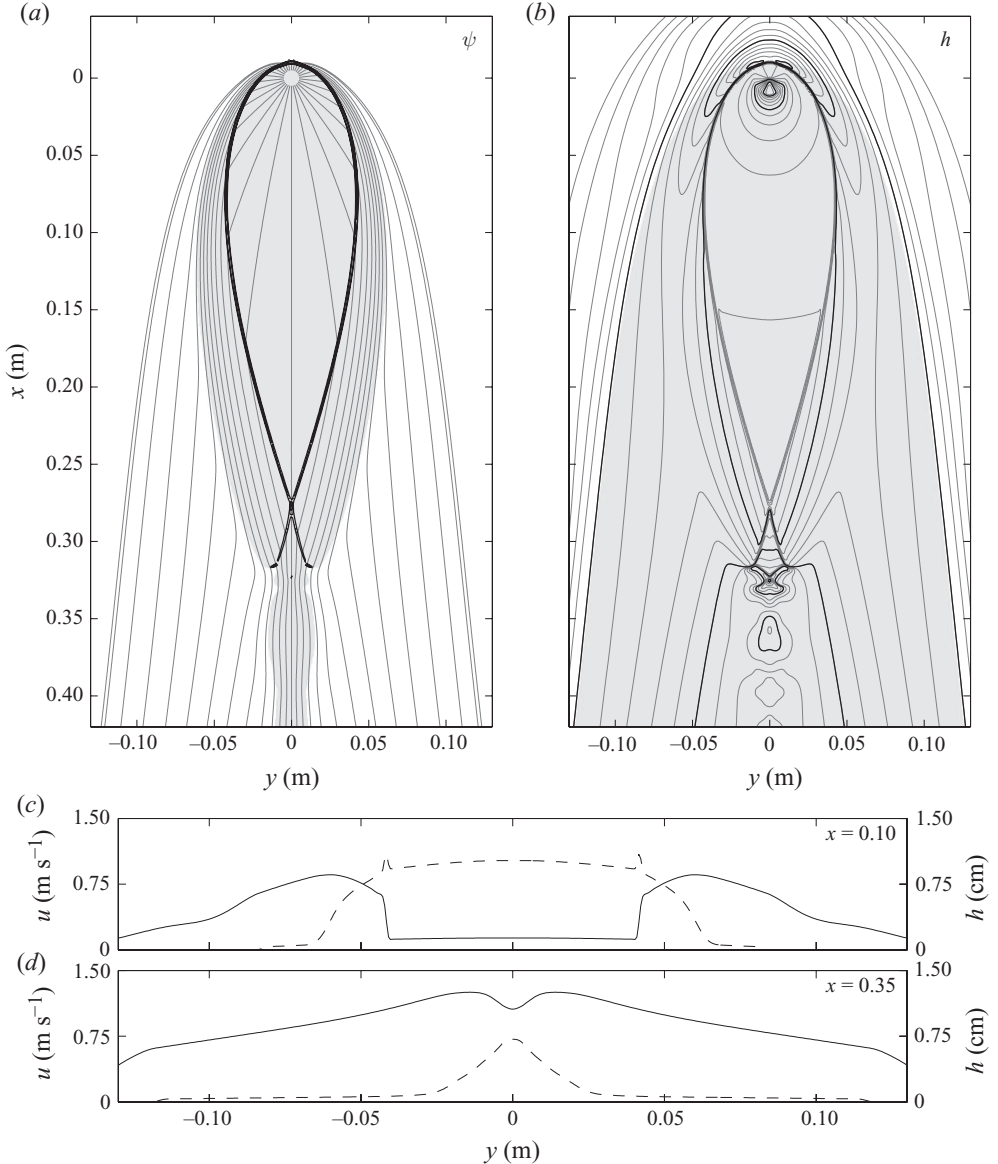


FIGURE 8. Steady-state numerical solution for $\zeta = 26.7^\circ$, $u_{jet} = 0.99 \text{ m s}^{-1}$ and $D = 15 \text{ mm}$. The axes correspond to the same regions shown in figures 2 and 4. In (a), the shading indicates supercritical flow ($Fr > 1$). The grey lines are streamlines, and the thick black line indicates the region of strongly converging flow velocity, an identifying feature of the shock. In (b), contours are of flow height, at intervals of 1 mm, with dark contours at intervals of 5 mm. Shading indicates the flowing region of material. Figures (c) and (d) show cross-sectional plots of flow variables, for $x = 0.1 \text{ m}$ and $x = 0.35 \text{ m}$, respectively. Downslope velocity u is indicated by a dashed line and flow depth h by a solid line.

motion blur. The streamlines in this region, which follow the line of the shock, further resemble the experimental flow. The structure of these streams is visible in figure 8(c), which shows the values of the flow variables u (dashed line) and h (solid line) along a cross-section at $x = 0.1 \text{ m}$, through the closed shock. Inside the shock (which occurs at $y = \pm 0.04 \text{ m}$), $u \approx 0.99 \text{ m s}^{-1}$ as expected, and $h \approx 1.3 \text{ mm}$, close to the experimental

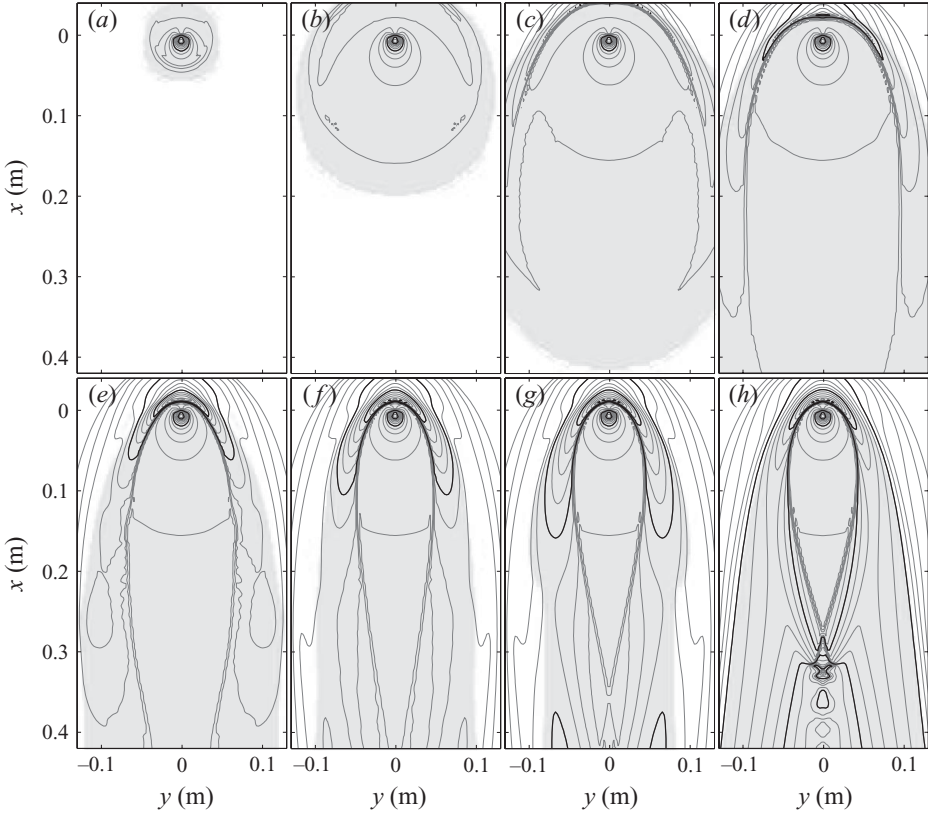


FIGURE 9. Time sequence of the numerical solution of figure 8, with $\zeta = 26.7^\circ$, $u_{jet} = 0.99 \text{ m s}^{-1}$ and $D = 15 \text{ mm}$. Contours and shading have the same meaning as in figure 8(b). The times after jet impact in each sub-figure are in the same ratio as those in figure 3: (a) 0.02, (b) 0.1, (c) 0.26, (d) 0.50, (e) 1.0, (f) 1.26, (g) 1.76, (h) steady-state. A movie showing the time-dependent behaviour of this solution is available with the online version of this paper.

estimate of $h = 1 \text{ mm}$. Across the shock, while h increases rapidly to about 6.5 mm , u is nearly continuous. (The peak in u at the location of the shock is a numerical artifact caused by the non-conservative form of u .) The continuity of u is due to the jump relation (2.9) which implies that velocity tangential to the shock (which is nearly in the downslope direction at $x = 0.1 \text{ m}$) is continuous. It is this continuity of tangential velocity which causes the fast-moving streams of material to exist outside the shock. A substantial shear exists in the stream, as u decreases by an order of magnitude to approximately 0.05 m s^{-1} over 2.5 cm . At the vertex of the shock, the numerical solution exhibits a pair of shock reflections, leading to a weakening stream of shock interactions and reflections in the supercritical flow downstream of the shock vertex. The structures of these shocks resemble those described for supercritical shallow-water flows by Akers & Bokhove (2008). Experimentally, the flow in the region below the shock vertex is complicated by the formation of a spout, which is outside the scope of the thin-layer model (Edwards *et al.* 2008), but some evidence of a shock reflection, forming a triangular region downstream of the shock vertex, can be seen in figure 2. The extended chain of shocks below this is not observed in our experimental flows.

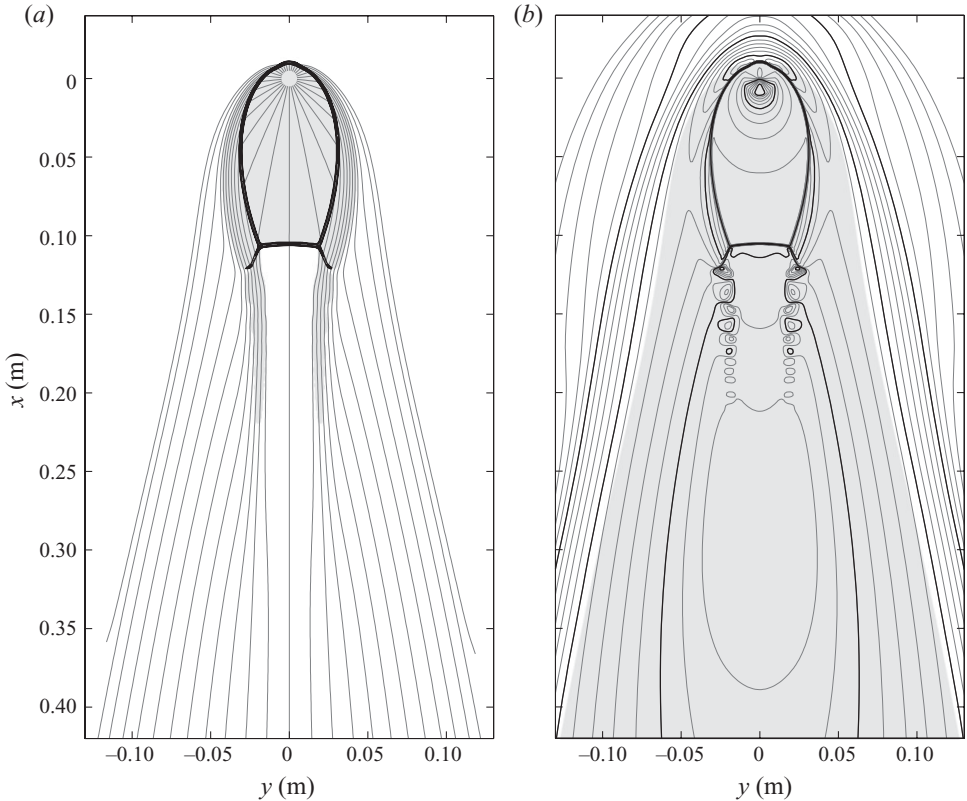


FIGURE 10. Numerical solution for $\xi = 24.5^\circ$, $u_{jet} = 0.99 \text{ m s}^{-1}$ and $D = 15 \text{ mm}$. The flow has reached the steady state. The meaning of contours and shading for (a) and (b) is as in figure 8(a) and (b) respectively. A movie showing the evolution to this steady state is available at journals.cambridge.org/flm.

The flow thickness is shown by the contours in figure 8(b). The rapid increase in flow height across the teardrop-shaped shock is evident, as is the variation in thickness downstream of the shock vertex caused by the chain of shock interactions. The shaded region in figure 8(b) indicates flowing material. Surrounding and upslope of the flowing region, a region of stationary (unshaded) material is present. This is consistent with the location of stationary material in experimentally observed flows; material above the point of impingement is held stationary by the pressure of the upstream flow (figure 6), while a thin layer of stationary material with $h \leq h_{stop}$ surrounds the flowing region further down the plane (figure 2).

Figure 8(d) shows a cross-section at $x = 0.35 \text{ m}$, through the flow just downstream of the shock. For $0.03 < |y| < 0.125 \text{ m}$, u varies between 0.08 and 0.04 m s^{-1} . These velocities are within 20 % of the velocity of a steady uniform down-slope flow of the same thickness profile (obtained from h by solving (4.4) for u). Along the centreline of the flow, at $x = 0.35 \text{ m}$, the velocity is significantly larger at 0.7 m s^{-1} , eight times faster than the steady uniform flow speed. This is part of the supercritical region downstream of the shock vertex in figure 8(a), and reflects the rapidly moving stream observed in experiments. Far downstream, the numerical prediction of centreline velocity is 0.12 m s^{-1} , close to the experimental measurement of 0.11 m s^{-1} .

The time-dependent flow which leads to the steady state shown in figure 8 is shown in figure 9. The evolution to the steady solution bears a strong resemblance to the experimentally observed transient flow in figure 3: the material upstream of the impingement point stagnates and a shock forms, separating the inner fast-moving region from the slower flow surrounding it. The shock propagates downslope and wraps around the radial flow region, eventually closing at the downstream vertex. This propagates back towards the impingement point until the flow reaches a steady state. As in the experimental observations, a region of stationary particles is formed outside the flowing region in the numerical solution in the initial stages of the flow (figure 8*a–c*).

5.2. Blunted shock

Figure 10 shows a numerical solution at a lower inclination angle of $\zeta = 24.5^\circ$, resembling the blunted shock regime observed experimentally (figure 4). In order to produce a comparable blunted shock, the slope angle in figure 10 is 0.9° lower than that in figure 4; we discuss this discrepancy in § 5.3. The shock in figure 10 is not closed at a sharp vertex, but by a curved shock lying across the slope. A transition from supercritical to subcritical flow occurs across this cross-slope shock, indicated by the shading in figure 10(*a*). For the thin-layer granular avalanche equations (2.2)–(2.4), Gray & Cui 2007 (p. 121) show that such a transition implies that the shock is a strong shock. The strong shock meets the pair of shocks surrounding the point of impingement at shock interaction points. Each of these is the triple point of a Mach reflection, with the strong cross-slope shock forming the Mach stem. Two further line discontinuities are generated at each triple point, one a reflected shock and another a contact discontinuity. These are visible in figure 10(*a*), the reflected shock as a thick black line, and the contact discontinuity as the inner edge of the two streams of supercritical flow which continue downstream of the strong shock. As in the case of a teardrop shock solution, a chain of weaker shock reflections exists in these two streams, which are too weak to be indicated as shocks on figure 10(*a*), but are clearly visible in the flow height contours of figure 10(*b*). The flow downstream of the strong shock was measured to be 0.07 m s^{-1} in the experiment of figure 4. The numerical simulation is consistent with this, predicting $u = 0.055 \text{ m s}^{-1}$ on the centreline immediately downstream of the shock at $x = 0.11 \text{ m}$, rising to $u = 0.081 \text{ m s}^{-1}$ at $x = 0.25 \text{ m}$.

A feature shown clearly in figure 10(*a*) (and which is present, but less clear, in figure 8*a*) is the structure of the two streams surrounding the shock. Within the region of the stream, the flow is supercritical (shaded in figure 10*a*) and streamlines are nearly parallel to the shock. This phenomenon is caused by the effect of the shock on the flow velocity: the rapid decrease in velocity normal to the shock as the material goes through the shock, together with the continuity of velocity tangential to the shock, results in material that has been through the shock travelling nearly tangential to it. Outside of the supercritical streams, the streamlines diverge sharply from being parallel to the shock, and assume their form for the flow far downstream.

One difference between the numerical solutions and experimental observations of figures 4 and 10, respectively is in the presence of a shock interaction point in the solution of the model equations, where instead a strongly curved shock is observed experimentally. This is likely to be due to either an effect of the granular rheology, or to the three-dimensional breaking wave observed at the shock in experiments. A related feature in experimental flows, not present in numerical solutions, is the thin trench in the flow which persists downstream. We attribute the formation of the trench

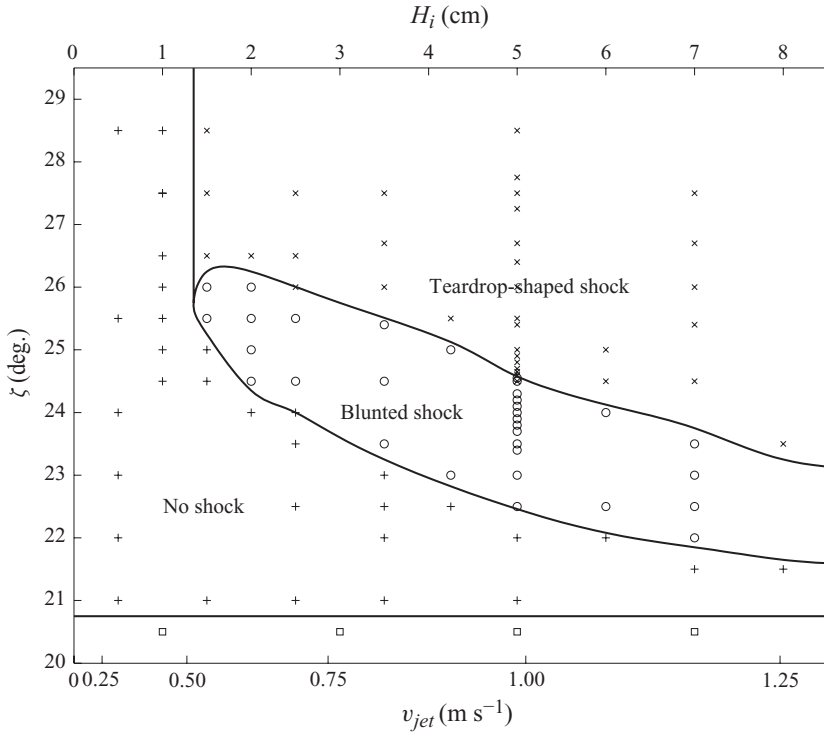


FIGURE 11. Numerical phase diagram, showing the dependence of flow regime on u_{jet} and ζ , for $D = 15$ mm. As before, teardrop-shaped shocks are indicated by crosses (\times), blunted shocks by circles (\circ) and steady flows showing no shock by plus signs ($+$). Time-dependent flows are represented by squares (\square). All flows for $\zeta \gtrsim 21^\circ$ are steady.

in experiments to the complex three-dimensional flow in the shock region, which is not present in the depth-integrated model. However, even if a perturbation in height is introduced artificially into a time-dependent numerical solution, the perturbation will dissipate in a wave-like manner; by contrast, in experimental flows, the perturbation persists and is advected downstream. This suggests that the persistence of the trench is due to the actual rheology differing from the modelled lithostatic pressure distribution. The lack of disturbance of the trench, and of grains on the surface of thicker experimental flows such as that in figure 4, suggests that very little shear occurs near the surface, the shear being concentrated instead in a thin region at the base.

5.3. Dependence on ζ and u_{jet}

A phase diagram of flow regimes observed in the numerical solutions for $D = 15$ mm is shown in figure 11, which is comparable to the experimental phase diagram in figure 5. The four regimes of flow (unsteady flows, steady flows without a shock, steady teardrop-shaped shocks and steady blunted shocks) and their relative locations on the phase diagram are all reproduced by the shallow-flow model.

The numerical results are parameterised by u_{jet} , the speed of flow exiting the impingement region in (4.16). In the experiments, this velocity is unknown, but is dependent on the funnel height H_f . To aid comparison between figures 5 and 11, we plot figure 11 with the effective funnel height H_i required to generate flow exiting the impingement region at u_{jet} . Assuming a freely falling jet (in which the grain acceleration is g) and no loss of energy in the impingement region, this effective

height is

$$H_i = \frac{u_{jet}^2}{2g}. \quad (5.3)$$

The energy loss in the impingement region causes H_i to be significantly smaller than the corresponding experimental H_f : for a flow speed exiting the impingement region of 0.99 ms^{-1} as measured for the flow in figure 2, $H_i \approx 5 \text{ cm}$, whereas $H_f = 30 \text{ cm}$.

The model solutions reproduce the experimental result of a single inclination angle dividing steady and unsteady flows, and (for sufficiently large ζ) a single value of H_i separating flows with teardrop-shaped shocks and flows with no shocks. The numerical solutions also correctly predict that as H_i increases, blunted shocks are observed over a shallower range of slope angles, though this effect is more pronounced in numerical simulations than in experiments. The overestimate could be attributed to an increasing proportion of the energy of the granular jet being dissipated in the impingement region with increasing H_i . In general, the numerical solutions predict the occurrence of flow regimes at lower slope angles than those measured experimentally. Such a difference is to be expected, since our grains and the inclined plane surface roughness are not identical to those used by Pouliquen & Forterre (2002) in the measurements of the friction law.

While the regimes of teardrop-shaped and blunted shocks are closely reproduced by numerical solutions, the regimes of unsteady flow and of steady flow without a shock are modelled less well. Experimentally, when H_i is sufficiently low, the flow velocity is too small to create a clear shock and a diffuse transition to downslope flow is observed. In the numerical solutions, rheological effects that would cause the shocks to become diffuse are not modelled, and we do not observe these smooth solutions. Instead, the size of the predicted shock continues to decrease with H_i , to the point where the shock reaches the diameter of the impinging jet. In figure 11, we mark solutions as having no shock if either the shock width or length is smaller than the diameter of the impinging jet. Flows with no shock also occur experimentally when ζ is sufficiently small, in which case the flow is subcritical everywhere, including at the point of impingement. In numerical solutions of these flows, a subcritical flow with no shocks is observed everywhere in the domain, apart from that in the impingement region, where the model of § 4.2 is applied. While this model of the impinging jet is not appropriate for flows which are subcritical at the impingement point, it nonetheless provides us the correct mass flux to a subcritical flow.

The regimes in the numerical phase diagram are robust to changes in the parameters of the friction law. While the values of ζ and H_i for which different regimes occur vary with the details of the friction law, as does the size of the shock, the occurrence and relative position in the phase diagram of the four flow regimes are insensitive to the precise formulation. This is consistent with the experimental observation of blunted and tear-drop-shaped shocks in a range of granular materials, particle sizes and rough surfaces.

Figure 12 shows numerical predictions and experimental measurements of the shock length (the distance from the impingement point to the lowest point of the shock). The experimental results are for $H_f = 30 \text{ cm}$, and the numerical solutions at the corresponding $u_{jet} = 0.99 \text{ m s}^{-1}$.

An approximately linear relationship between shock length and slope angle is observed experimentally. The numerical predictions are in quantitative agreement with experimental measurements at steeper slope angles, where the flow is well into

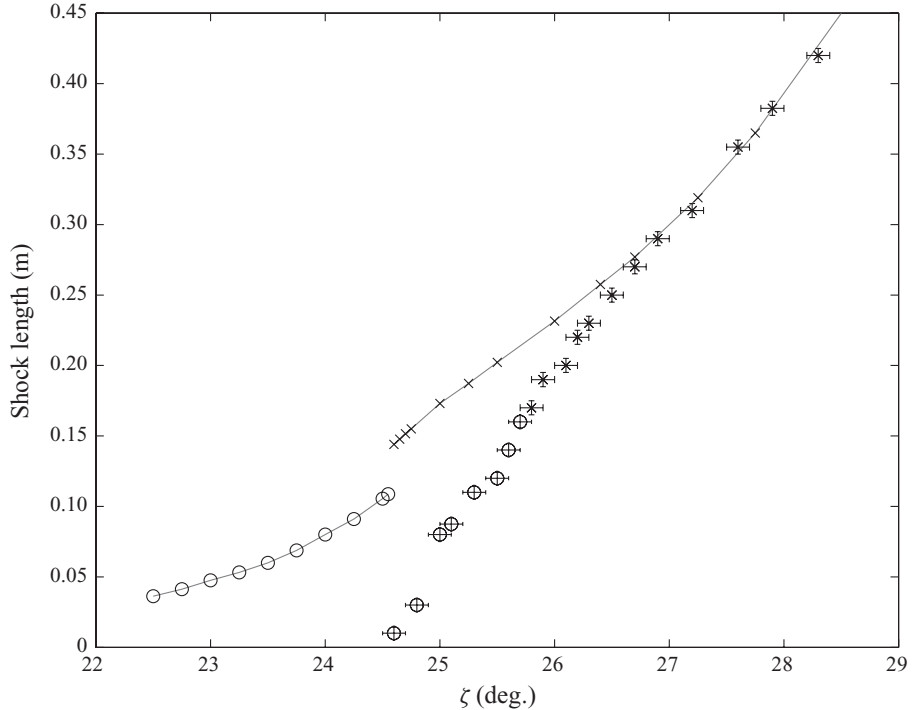


FIGURE 12. Experimental measurements and numerical predictions of the shock length, against slope angle, for $D = 15$ mm, $H_f = 30$ cm (experimental) and $u_{jet} = 0.99$ m s $^{-1}$ (numerical). Experimental measurements are indicated by symbols with error bars, and numerical results are joined by a grey line. A cross (\times) indicates a teardrop-shaped shock, and a circle (\circ) a blunted shock.

the teardrop-shaped shock regime. At lower slope angles, the discrepancy between numerical and experimental results at lower slope angles is due, as before, to the difference between particle and surface properties in our experimental setup, and in that used to determine the friction law.

A notable feature of the model results is the discontinuous change in shock lengths that occurs at the transition between teardrop-shaped and blunted shocks ($\xi = 24.6^\circ$). No such discontinuity is evident in the experimental results. This reinforces the conclusion that, although the primary mechanism for the formation of blunted granular jumps is the presence of a Mach reflection, three-dimensional or rheological effects also play an important role.

6. Unsteady flows

The flows considered thus far have all tended quickly to a steady state after an initial transient flow. A range of flows are observed experimentally, below a critical slope angle ξ_0 , which do not tend to steady flow or which do so in a complex manner. This angle is insensitive to H_f (figure 5), but decreases with increasing D . At sufficiently low ξ , no steady flows are observed, for all H_f and D .

These observations are consistent with the hypothesis that unsteady flow behaviour is related to stationary material on the plane and the stick-slip behaviour encapsulated by the heights h_{start} and h_{stop} . Static uniform layers of material can exist on the plane at heights up to h_{start} . If the depth of flowing material is similar to or smaller than this,

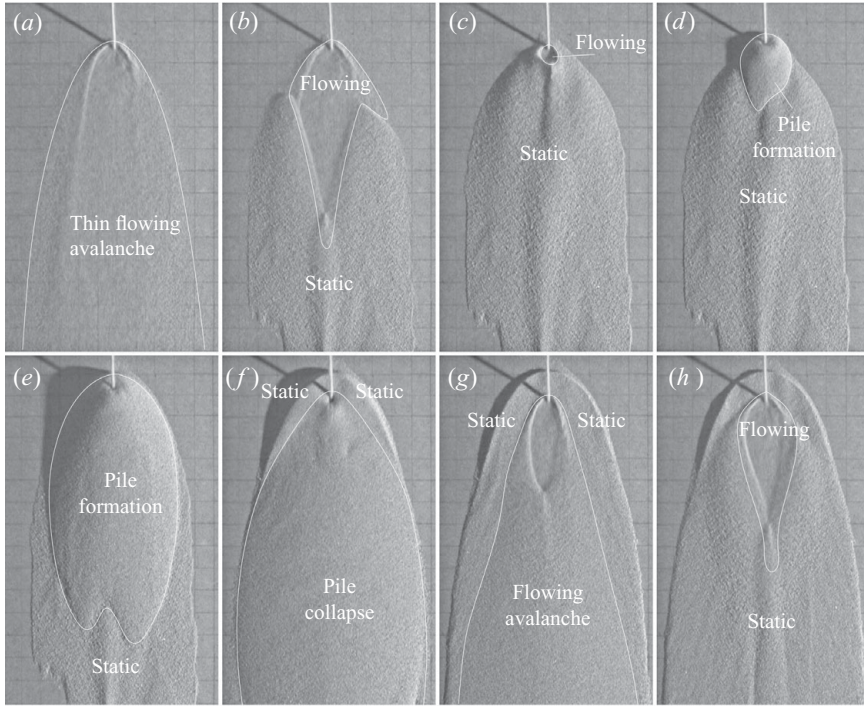


FIGURE 13. Unsteady flow, $\zeta = 26.5^\circ$, $H_f = 25\text{ cm}$, $D = 10\text{ mm}$. Material striking the plane in (a) spreads into a thin layer, as in figure 3(a). This layer slows downstream and becomes stationary (b), and the shock connecting the stationary to the flowing material propagates back towards the point of impingement (b–c). When the shock reaches the impingement point, the flow regime changes to the formation of a conical pile (d), which grows through avalanches down its flanks. A number of such avalanches occur (e), before a collapse of the pile occurs (f). This reforms the region of thin, radial flow around the impingement point and surrounding shock (g). The material downstream is arrested by friction, and the shock again propagates inwards and towards the point of impingement (h). A movie showing the evolution of this unsteady flow is available with the online version of this paper.

the effect of the static layer on the location and form of the flow becomes significant. From a steady-state flow, this situation can occur either through a decrease in mass flux (and correspondingly in h), or through a decrease in ζ , with a corresponding increase in h_{start} and h_{stop} .

For a given mass flux, a steady uniform flow has its thickness and velocity determined by mass conservation, and by the balance of forces

$$\mu(h, u) = \tan \zeta, \quad (6.1)$$

corresponding to $s_x = 0$ in (2.3). If the mass flux is sufficiently small, or the cross-slope width sufficiently large, the flow height h becomes less than h_{stop} and no steady solution exists. The flow regime entered in this case is one of unsteady avalanching.

A typical unsteady flow is shown in figure 13. Material downstream of the impingement region is arrested by friction to form a layer of stationary material on the plane, and two shocks propagate up towards the point of impingement (figure 13b). The two shocks connect, and a closed shock resembling that of the steady teardrop-shaped shock is formed, although in this case the shock continually propagates inwards towards the impingement point. The flowing region consists of

the thin radial flow surrounding the shock, and two supercritical streams of flow immediately outside the shock that were identified in the steady-state flows. Outside this, the flow is stationary. This flowing region contrasts with that seen in a one-dimensional propagating granular bore, in which the grains are brought to rest rapidly by the shock (Gray *et al.* 2003). In the oblique shocks of 13(b), only the flow velocity normal to the shock is brought to zero, leaving tangentially flowing streams of material in the thicker flow outside the closed jump. The collision of these streams at the vertex of the shock creates a stream of moving grains downstream of the vertex (shown in figure 13b), which deposits a ridge of stationary material (figure 13b–e). Up to this point, the impingement region and shallow-layer flow models presented are appropriate, and can reproduce the main features of the flow.

When the shock reaches the impingement point (figure 13c), the flow switches to a new regime of conical pile formation (figure 13d), in which the flow is no longer shallow. Material in the falling jet is slowed rapidly by impact with other material on the plane, and acts simply as a mass source at the top of the conical pile. The flow is thus very insensitive to H_f once in this regime. The pile grows through unsteady avalanching down its flanks. Avalanches are concentrated on the downslope flank of the pile, and are approximately periodic, with a period of the order a few seconds, though the position on the flank and temporal length of each avalanche vary.

Unlike pile formation on a horizontal plane, where the size of the pile grows indefinitely, a spontaneous collapse of the pile occurs on an inclined plane. Figure 13(e) shows the pile just before this occurs. The collapse causes a large mass of material to flow down the plane (figure 13f), re-mobilising the existing static layer. As a consequence of this collapse, a new region of fast radial flow surrounded by a closed shock forms around the impingement point. Uphill and to the sides of the impingement point, there remains a deep pile of stationary material, the remnants of the conical pile. The flow from the collapsed part of the conical pile thins as it spreads, and becomes static as h drops below h_{stop} . As before, this causes the shock to propagate inwards towards the impingement point, and a new conical pile is formed. The sequence of conical pile formation, collapse, flow stagnation and inward shock propagation may repeat for several tens of cycles.

The initiation of collapse of the growing conical pile is nearly simultaneous across the whole pile, occurring within one frame of video (1/25th second), which corresponds to a rate of information propagation of $\gtrsim 5 \text{ m s}^{-1}$. This is much faster than the gravity wave speed of 0.7 m s^{-1} predicted by the hyperbolic equations (2.2)–(2.4), indicating that the mechanism of collapse is not captured by the depth-averaged model. The collapse does not occur at a well-defined pile size; the onset appears to be very sensitive to the properties of the pile, possibly to the internal micro-structure of the grains.

Small asymmetries can be seen in figures 13(d) and 13(e), which can be attributed to variations in the height of the static material. A much greater asymmetry occurs occasionally in the collapse of the conical pile. This asymmetric collapse is due to the ridge of material seen in figure 13(b–e), which has the effect of supporting the central part of the conical pile against collapse. As a result, the collapse can occur on only one side of the pile. The resulting flow, shown in figure 14, consists of an asymmetric flowing region with several shocks. The flowing region is bounded by thick stationary material from the conical pile, which diverts the flow near the impingement region to one side, and by a thinner layer of static material on the inclined plane, which restricts the downslope flow to a narrow channel. The flow is nearly steady: the restriction of the width of flowing material allows the flowing layer downstream to have a depth

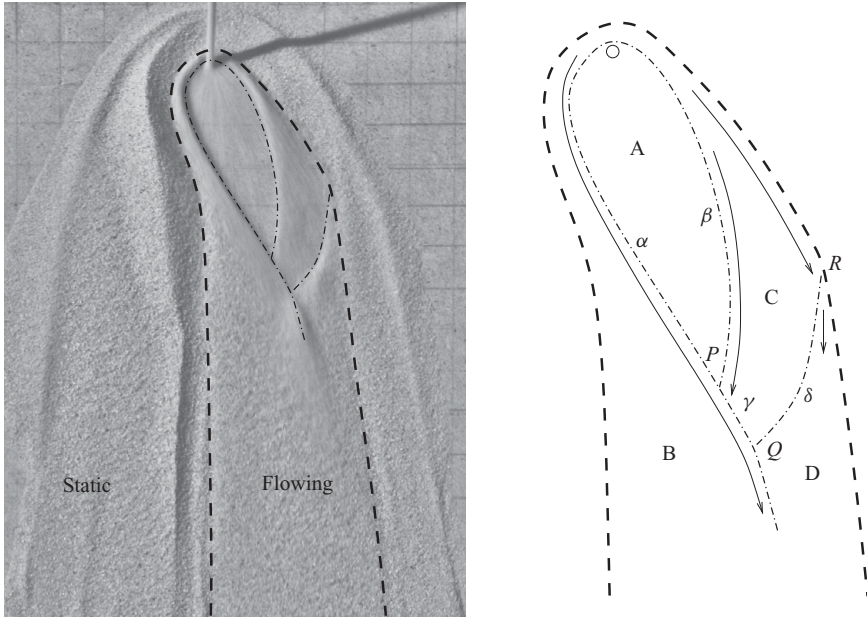


FIGURE 14. Asymmetric flow, $\zeta = 26.4^\circ$, $H_f = 9\text{ cm}$, $D = 8\text{ mm}$. Dashed lines indicated the boundary of the flowing region; thin dot-dash lines indicate the location of shocks. The flow is quasi-steady, in the sense the time-dependence is through slow evolution of the boundary between static and flowing grains.

greater than h_{stop} , and thus be in steady uniform flow. A very slow evolution of the flow is observed, caused by erosion of the static grains, and deposition of the flowing ones, at the boundary between flowing and static material.

The shock structure in figure 14 differs from that seen in the teardrop and blunted cases. The shock surrounding region A is asymmetric, with a greater mass flux from regions A to B across shock α than that from regions A to C across shock β . Beyond the point P , the flow in region C converges with the thicker flow of region B, forming the shock γ between the two regions. Shock δ , separating regions C and D, originates at the point R , where the boundary between flowing and static grains is sharply curved. This is an oblique shock, analogous to that found in the case of a compression ramp in supersonic gas dynamics (Courant & Friedrichs 1977) and in converging channels of flowing granular material (Gray & Cui 2007). A second shock interaction point is formed at Q .

7. Conclusion

The flow generated by impingement of a granular jet on an inclined plane, while having similarities with its fluid counterpart, exhibits a range of behaviour specific to granular materials. Two distinct steady-state flow regimes displaying closed granular jumps have been found, one with a teardrop-shaped shock and one with a smooth, ‘blunted’ shock. In these two regimes, the principal features of the flow, listed from the point of impingement outwards, are a fast-moving region of thin radial flow, a closed granular jump, rapid streams of material flowing nearly tangentially to the shock, a region of slower downslope flow and static material outside the flowing region. The two regimes differ in the supercritical or subcritical nature of the thicker

flow surrounding the shock; fully supercritical flow leads to a teardrop-shaped shock, whereas subcritical flow surrounding the downstream part of the shock leads to a blunted shock.

These flows have been modelled through a shallow-layer approximation, leading to a system of hyperbolic equations. The concepts of sub- or supercritical flow and shock waves which result from these equations are fundamental to an understanding of the flow. Numerical solutions of the model equations reproduce the phase diagram of the solution regimes, and quantitatively predict features such as flow velocity and the shock length in the regime of steady teardrop-shaped shocks. The three-dimensional breaking wave observed in blunted shocks is outside the scope of the depth-averaged model, but the overall form of flow is nonetheless correctly reproduced, displaying quantitative agreement with the measured flow velocity.

The steady granular jumps, and the radial flow within them, are governed primarily by conservation of mass and momentum. Outside the shock, in the slower downslope flow, the basal friction and gravity source terms play an important role. The balance of these forces governs the flow far downstream, and influences the form of the granular jump through control of the flow on the downstream side of the shock.

At sufficiently low slope angles, there is no steady balance between gravity and friction in the downslope flow. Instead, the hysteretic nature of the transition between flowing and stationary material, encapsulated in the functions h_{start} and h_{stop} leads to oscillatory behaviour and periodic avalanching. The exact mechanism is unclear, however, for transition between stationary and moving flow (involved in the erosion and deposition of static material), and for the sudden collapse of the conical pile. Such regimes are known to exhibit complex dynamics (Pouliquen & Forterre 2002), and are likely dependent on details of the grain micro-structure.

C.J. acknowledges support from an NERC DTG NE/G523747/1 and an EPSRC DTA. J.M.N.T.G. was supported by an NERC grant NE/E003206/1 and an EPSRC Advanced Research Fellowship GR/S50052/01 & GR/S50069/01.

Supplementary movies are available at journals.cambridge.org/film.

REFERENCES

- AKERS, B. & BOKHOVE, O. 2008 Hydraulic flow through a channel contraction: Multiple steady states. *Phys. Fluids* **20**, 056601.
- BOUDET, J. F., AMAROUCHENE, Y., BONNIER, B. & KELLAY, H. 2007 The granular jump. *J. Fluid Mech.* **572**, 413–431.
- BRENNEN, C. E., SIECK, K. & PASLASKI, J. 1983 Hydraulic jumps in granular material flow. *Powder Technol.* **35**, 31–37.
- BUSH, J. W. M. & ARISTOFF, J. M. 2003 The influence of surface tension on the circular hydraulic jump. *J. Fluid Mech.* **489**, 229–238.
- BUSH, J. W. M. & HASHA, A. E. 2004 On the collision of laminar jets: fluid chains and fishbones. *J. Fluid Mech.* **511**, 285–310.
- COURANT, R. & FRIEDRICHHS, K. O. 1977 *Supersonic Flow and Shock Waves*. Springer.
- COURANT, R. & HILBERT, D. 1962 *Methods of Mathematical Physics*. Interscience.
- CUI, X., GRAY, J. M. N. T. & JÓHANNESSEN, T. 2007 Deflecting dams and the formation of oblique shocks in snow avalanches at Flateyri, Iceland. *J. Geophys. Res. – Earth Surf.* **112** (F4), F04012.
- DOYLE, E. E., HUPPERT, H. E., LUBE, G., MADER, H. M. & SPARKS, R. S. J. 2007 Static and flowing regions in granular collapses down channels: Insights from a sedimenting shallow water model. *Phys. Fluids* **19**, 106601.
- EDWARDS, C. M., HOWISON, S. D., OCKENDON, H. & OCKENDON, J. R. 2008 Non-classical shallow water flows. *IMA J. Appl. Maths.* **73** (1), 1–21.

- EGLIT, M. E. 1983 Some mathematical models of snow avalanches. In *Advances in Mechanics and the Flow of Granular Materials* (ed. M. Shahinpoor), p. 577. Zellerfeld and Gulf.
- EGLIT, M. E., KULIBABA, V. S. & NAAIM, M. 2007 Impact of a snow avalanche against an obstacle. Formation of shock waves. *Cold Reg. Sci. Technol.* **50** (1–3), 86–96.
- FORTERRE, Y. & POULIQUEN, O. 2003 Long-surface-wave instability in dense granular flows. *J. Fluid Mech.* **486**, 21–50.
- GRAY, J. M. N. T. & ANCEY, C. 2009 Segregation, recirculation and deposition of coarse particles near two-dimensional avalanche fronts. *J. Fluid Mech.* **629**, 387–423.
- GRAY, J. M. N. T. & CUI, X. 2007 Weak, strong and detached oblique shocks in gravity-driven granular free-surface flows. *J. Fluid Mech.* **579**, 113–136.
- GRAY, J. M. N. T. & HUTTER, K. 1997 Pattern formation in granular avalanches. *Continuum Mech. Thermodyn.* **9** (6), 341–345.
- GRAY, J. M. N. T., TAI, Y. C. & NOELLE, S. 2003 Shock waves, dead zones and particle-free regions in rapid granular free-surface flows. *J. Fluid Mech.* **491**, 161–181.
- GRAY, J. M. N. T., WIELAND, M. & HUTTER, K. 1999 Free surface flow of cohesionless granular avalanches over complex basal topography. *Proc. R. Soc.* **455**, 1841–1874.
- GRIGORYAN, S. S., EGLIT, M. E. & YAKIMOV, Y. L. 1967 New state and solution of the problem of the motion of snow avalanche. *Tr. Vysokogornogo Geofizich Inst.* **12**, 104–113.
- GRUBER, U. & BARTELT, P. 2007 Snow avalanche hazard modelling of large areas using shallow water numerical methods and GIS. *Environ. Model. Softw.* **22** (10), 1472–1481.
- HÁKONARDÓTTIR, K. M. & HOGG, A. J. 2005 Oblique shocks in rapid granular flows. *Phys. Fluids* **17**, 077101.
- HASSON, D. & PECK, R. E. 1964 Thickness distribution in a sheet formed by impinging jets. *AICHE J.* **10** (5), 752–754.
- IVERSON, R. M. 1997 The physics of debris flows. *Rev. Geophys.* **35** (3), 245–296.
- IVERSON, R. M. & DENLINGER, R. P. 2001 Flow of variably fluidized granular masses across three-dimensional terrain: Part 1. Coulomb mixture theory. *J. Geophys. Res.* **106**, 537–552.
- JIANG, G-S. & TADMOR, E. 1998 Nonoscillatory central schemes for multidimensional hyperbolic conservation laws. *SIAM J. Sci. Comput.* **19** (6), 1892–1917.
- KATE, R. P., DAS, P. K. & CHAKRABORTY, S. 2007 Hydraulic jumps due to oblique impingement of circular liquid jets on a flat horizontal surface. *J. Fluid Mech.* **573**, 247–263.
- LAJEUNESSE, E., MANGENEY-CASTELNAU, A. & VILOTTE, J. P. 2004 Spreading of a granular mass on a horizontal plane. *Phys. Fluids* **16**, 2371.
- LEVEQUE, R. J. 1992 *Numerical Methods for Conservation Laws*. Birkhäuser.
- LEVEQUE, R. J. 2002 *Finite Volume Methods for Hyperbolic Problems*. Cambridge Texts in Applied Mathematics, p. 31. CUP.
- LIU, A. J. & NAGEL, S. R. 1998 Jamming is not just cool any more. *Nature* **396** (6706), 21–22.
- LUBE, G., HUPPERT, H. E., SPARKS, R. S. J. & HALLWORTH, M. A. 2004 Axisymmetric collapses of granular columns. *J. Fluid Mech.* **508**, 175–199.
- MITCHELL, J. K. & SOGA, K. 2005 *Fundamentals of Soil Behavior*. Wiley.
- NESSYAHU, H. & TADMOR, E. 1990 Non-oscillatory central differencing for hyperbolic conservation laws. *J. Comput. Phys.* **87** (2), 408–463.
- POULIQUEN, O. 1999a On the shape of granular fronts down rough inclined planes. *Phys. Fluids* **11**, 1956.
- POULIQUEN, O. 1999b Scaling laws in granular flows down rough inclined planes. *Phys. Fluids* **11** (3), 542–548.
- POULIQUEN, O. & FORTERRE, Y. 2002 Friction law for dense granular flows: application to the motion of a mass down a rough inclined plane. *J. Fluid Mech.* **453**, 133–151.
- RAJCHENBACH, J. 2000 Granular flows. *Adv. Phys.* **49** (2), 229–256.
- RAYLEIGH, LORD 1914 On the theory of long waves and bores. *Proc. R. Soc. A* **90** (619), 324–328.
- RERICHA, E. C., BIZON, C., SHATTUCK, M. D. & SWINNEY, H. L. 2002 Shocks in supersonic sand. *Phys. Rev. Lett.* **88** (1), 6338.
- ROUSE, H. 1949 *Engineering Hydraulics*. Wiley.
- ROYER, J. R., EVANS, D. J., OYARTE, L., GUO, Q., KAPIT, E., MÖBIUS, M. E., WAITUKAITIS, S. R. & JAEGER, H. M. 2009 High-speed tracking of rupture and clustering in freely falling granular streams. *Nature* **459** (7250), 1110–1113.

- SAVAGE, S. B. 1979 Gravity flow of cohesionless granular materials in chutes and channels. *J. Fluid Mech.* **92** (01), 53–96.
- SAVAGE, S. B. & HUTTER, K. 1989 The motion of a finite mass of granular material down a rough incline. *J. Fluid Mech.* **199**, 177–215.
- SCHACH, W. 1934 Umlenkung eines freien Flüssigkeitsstrahles an einer ebenen Platte. *Ingenieur Archiv* **5** (4), 245–265.
- STARON, L. & HINCH, E. J. 2005 Study of the collapse of granular columns using two-dimensional discrete-grain simulation. *J. Fluid Mech.* **545**, 1–27.
- TAI, Y. C., NOELLE, S., GRAY, J. M. N. T. & HUTTER, K. 2001 An accurate shock-capturing finite-difference method to solve the Savage Hutter equations in avalanche dynamics. *Ann. Glaciol.* **32** (1), 263–267.
- TAI, Y. C., NOELLE, S., GRAY, J. M. N. T. & HUTTER, K. 2002 Shock-capturing and front-tracking methods for granular avalanches. *J. Comput. Phys.* **175** (1), 269–301.
- TAYLOR, G. 1966 Oblique impact of a jet on a plane surface. *Phil. Trans. R. Soc. A* **260** (1110), 96–100.
- TAYLOR, G. I. 1960 Formation of thin flat sheets of water. *Proc. R. Soc. Lond. Ser. A, Math. Phys. Sci.* **259** (1296), 1–17.
- THORPE, S. A. & KAVCIC, I. 2008 The circular internal hydraulic jump. *J. Fluid Mech.* **610**, 99–129.
- VREMAN, A. W., AL-TARAZI, M., KUIPERS, J. A. M., VAN SINT ANNALAND, M. & BOKHOVE, O. 2007 Supercritical shallow granular flow through a contraction: experiment, theory and simulation. *J. Fluid Mech.* **578**, 233–269.
- WATSON, E. J. 1964 The radial spread of a liquid jet over a horizontal plane. *J. Fluid Mech.* **20** (03), 481–499.
- WEIYAN, T. 1992 *Shallow Water Hydrodynamics*. Elsevier.
- ZHAO, J. & KHAYAT, R. E. 2008 Spread of a non-Newtonian liquid jet over a horizontal plate. *J. Fluid Mech.* **613**, 411–443.